



Viscous fingering regimes in elasto-visco-plastic fluids



A. Eslami, S.M. Taghavi*

Department of Chemical Engineering, Laval University, Quebec, QC, Canada, G1V 0A6, Canada

ARTICLE INFO

Article history:

Received 9 September 2016

Revised 4 February 2017

Accepted 27 March 2017

Available online 30 March 2017

Keywords:

Saffman–Taylor instability

Viscous fingering

Yield stress

Elasticity

Shear-thinning

Inertia

ABSTRACT

We experimentally study the Saffman–Taylor instability of air invasion into a non-Newtonian fluid (i.e., Carbopol solution) in a rectangular Hele–Shaw cell. In addition to viscous features, the non-Newtonian fluid used exhibits yield stress, shear-thinning as well as elastic behaviors. The key dimensionless parameters that govern the various flow regimes are the Bingham number (Bn), the capillary number (Ca), the Weber number (We), the Weissenberg number (Wi), the channel aspect ratio ($\delta \gg 1$), and the shear-thinning power-law index (n). Three main flow regimes are observed, i.e., a *yield stress* regime, a *viscous* regime and an *elasto-inertial* regime. We present a detailed description for each regime and quantify their transition boundaries versus dimensionless groups. Some of the secondary flow aspects, e.g., the wall residual layer thickness and a *network structure* regime, have been also studied.

© 2017 Elsevier B.V. All rights reserved.

1. Introduction

Displacement flows are often vulnerable to interfacial instabilities in a variety of physical, chemical, biological, geophysical, and engineering systems. Of particular interest has been the *viscous fingering instability* or the *Saffman–Taylor instability* [72], which occurs when a less-viscous fluid displaces a more-viscous one, and refers to the appearance of finger-like interfacial patterns [30,49,85]. This interesting phenomenon is regarded as a representative of interfacial pattern formation and it has been studied numerous, from various perspectives, since it also frequently occurs in nature and industrial applications, such as sugar refining [28], carbon sequestration [15], enhanced oil recovery [60], oil well cementing [7], printing devices [77], chromatographic separations [70], coating [29], adhesives [57], and growth of bacterial colonies [5].

Viscous fingering in a traditional Hele–Shaw cell [30,49], made of two parallel flat plates with a small gap, has received much attention as a suitable framework to analyze interfacial instabilities in narrow confined passages, e.g., in porous media [30]. In the case of Newtonian fluids, the fluid motion in the Hele–Shaw cell is described by Darcy's law, which relates the two-dimensional averaged velocity across the gap \hat{V}^1 to the local pressure \hat{p} . Darcy's law is valid for laminar flows through porous media in the limit of low Reynolds number, Re (see [27,30]). The other governing equation of

the system is the mass conservation. These two equations are

$$\hat{v} = -\frac{\hat{b}^2}{12\hat{\mu}} \nabla \hat{p}, \quad (1)$$

$$\nabla \cdot \hat{v} = 0, \quad (2)$$

where \hat{b} and $\hat{\mu}$ denote the gap thickness and shear viscosity, respectively. Due to incompressibility, the pressure field satisfies Laplace's equation, $\nabla^2 \hat{p} = 0$. In order to determine the pressure jump across the interface, the Young–Laplace equation is used, i.e., $\Delta \hat{p} = \hat{\sigma} (1/\hat{R}_1 + 1/\hat{R}_2)$, where $\hat{\sigma}$ denotes the surface tension, and \hat{R}_1 and \hat{R}_2 are the interface curvature radius in the direction perpendicular to the parallel plates and that in the plane of motion, respectively. Since the gap thickness of the Hele–Shaw cell (\hat{b}) is small, it can be assumed that $1/\hat{R}_1 \approx 2/\hat{b}$, and that the larger radius of curvature, \hat{R}_2 , has a negligible effect [6,82]. Thus, the pressure jump over the interface is simplified to $\Delta \hat{p} \approx 2\hat{\sigma}/\hat{b}$.

Although various flow features, e.g., the wall wetting film thickness [61], the interface shape [75] and inertial effects [27,71], may require modifications to Darcy's law, this relation has been generally found suitable for Newtonian fluids. In particular, the shape and the width of the advancing finger (\hat{w}) can be obtained. For example, Saffman and Taylor [72] have shown in their classical work that \hat{w} is inversely proportional to the finger tip velocity (\hat{U}). They and other researchers have also shown that the relative finger width ($\lambda = \hat{w}/\hat{W}$) reaches a limiting value of $\sim 1/2$ at high finger tip velocities [30,34,72]. Despite many efforts, the applicability of Darcy's law to realistic non-Newtonian fluids has been more limited compared to Newtonian fluids [41,65].

* Corresponding author.

E-mail address: seyed-mohammad.taghavi@gch.ulaval.ca (S.M. Taghavi).

¹ In this paper we adopt the convention of denoting dimensional quantities with the \sim symbol and dimensionless quantities without.

The Saffman–Taylor instability problem for non-Newtonian fluids is not very well defined [47] due to complex rheological behaviors exhibited by these fluids. The effects of several key non-Newtonian properties have been investigated, such as yield stress [17,43,46,62], shear-thinning [9,25,83], shear-thickening [9,25,55] and elastic behaviors [31,47]. A new, diverse class of problems have been discovered [17,24,58], e.g., snowflake-like patterns [11] and branched, fractal, or fracture-like structures [32,39,59]. In particular, it has been found that shear-thinning effects induce dendritic patterns (with side branching) or crack-like patterns (with angular branches and sharp tips) [3,37]. Shear-thickening features may widen or narrow the finger width [33]. Viscoplastic properties have been found to strikingly modify Newtonian morphological patterns. For these fluids, Lindner et al. [43] have discovered the existence of a yield stress regime (with ramified structures) and a viscous regime (with a single finger) at small and moderate velocities. Maleki et al. [46] have also observed a side-branching regime at larger velocities. Numerical simulations of Ebrahimi et al. [21] confirmed some of the observed behaviors for these fluids. Finally, a fluid's thixotropy drastically affects the finger shape, leading to chaotic behaviors at longer times [22].

In general, in the displacement of a more viscous, wetting fluid by a less viscous, non-wetting fluid, the advancing finger leaves behind a wetting film of the displaced fluid on the wall of the flow geometry, the thickness of which has been the subject of many studies. For example, Bretherton [10] theoretically studied the film residual behind a flat interface for a Newtonian fluid flowing in a tube, at small capillary numbers, and found that the film is uniform and thin. For Newtonian fluids in the Hele-Shaw cell, the maximum film thickness is a function of $Ca^{2/3}$ [75,76], also reported by Bretherton [10] for the tube geometry. However, the film thickness in the Hele-Shaw cell may not be uniform as a result of the normal velocity variation along the interface [61,76]. Poslinski et al. [66] experimentally studied the displacement of a viscoplastic fluid by air in a horizontal tube and found that the film thickness is much larger compared to Newtonian fluids and it can increase up to 0.35 of the tube radius at high air flow rates. The film thickness for viscoplastic fluid depends on the tube geometry, finger shape and fluid properties, as numerically observed by Dimakopoulos and Tsamopoulos [20]. Through a combined theoretical and computational study, Allouche et al. [2] quantified the residual wall layer film thickness for viscoplastic for a 2D channel flow. Freitas et al. [26] have also shown that the yield stress value has a significant effect on the flow patterns and layer thickness, e.g., the film thickness decreases by an increase in the yield stress.

Although, as discussed, there are numerous studies in the literature addressing viscous finger of non-Newtonian fluids, there is hardly a clear picture of all the leading order flow regimes, especially versus the dimensionless parameters that govern the flow. This is due the fact that the complex rheology makes it hard to study the flow in generality as there is a wide range of parameters that control the flow (for example see Tables 1 and 2 showing the definitions & ranges of several dimensional/dimensionless parameters used in our study). Almost certainly, some of the non-Newtonian features are known in separate contexts, but our understanding is limited when they are present at the same time or compete with one another, which is the case in most non-Newtonian fluids. In addition, it is now accepted that many laboratory fluids, previously believed to be “ideal” in a sense that they only present a single non-Newtonian characteristic, in fact exhibit many competing non-Newtonian features simultaneously. A good example may be a Carbopol solution, which is shear-thinning, viscoplastic, weakly viscoelastic, although with no significant thixotropy [13,38,63,68]. In the light of the limitations of the literature mentioned, some of the key contributions of our study can be summarized as follows. (i) We characterize the regimes

of viscous fingering for a common laboratory fluid, i.e., Carbopol solution, exhibiting an interesting range of complex rheology. (ii) Through conducting a large number of experiments (~ 600), we are able to describe the flow regimes versus the dimensionless groups and delineate leading order boundaries between them. An effort has been devoted to find the best combination of the key dimensionless numbers to appropriately and clearly explain each regime and their corresponding transitions. (iii) While shedding further light on the previously-discovered regimes for viscoplastic fluids (e.g., [43,46]), i.e., the yield stress and viscous regimes, we also find for the first time an elasto-inertial flow regime, which corresponds to simultaneous presence of inertial and elastic effects, at high shear-rates. (iv) We provide an in-depth look into some of the secondary, interesting features of the flow, e.g., the wall residual film thickness and a network structure regime inside the finger domain. (v) Finally, there is a trend in recent studies to control the viscous fingering phenomena, for Newtonian fluids, through using various methods, e.g., non-uniformity of the geometry [1] (see also [54]), imposed flow rate variation [40], and elastic wall boundaries [64]. The extensions of these fascinating methods to control viscous finger for non-Newtonian fluids may only become possible when a clear, general picture of viscous fingering in non-Newtonian fluids becomes available. The current work may be a step in that direction.

The outline of the paper is as follows. In Section 2, the experimental setup, procedures, and fluid characterizations are discussed. Section 3 covers thoroughly the main flow regimes as well as some secondary flow behaviors. The paper concludes with a brief summary.

2. Experimental descriptions

Our experiments study was performed in a traditional, rectangular Hele-Shaw cell formed by two closely-spaced, smooth plexiglas plates. The channel dimensions and the flow parameters are given in Table 1. The plates of the cell were 1/2 inch thick to prevent bending. The plates were separated by a thin Nitrile Butadiene Rubber (NBR) spacer. The gap thickness was set using level screws distributed along both sides of the cell. This thickness was also controlled with digital caliper and a digital level meter. Rubber and level screws were used to prevent any fluid loss and control the gap thickness. A schematic of the experimental cell is shown in Fig. 1. The cell was initially filled with the displaced fluid, which was a Carbopol solution (Carbomer 940, Making Cosmetics Co.). Then, from the inlet of the cell, the displacing fluid (air) was injected. Light Emitting Diode (LED) stripes along with light diffuser panels were used to adjust the light. Light absorption calibrations were performed in a usual fashion. The advancing fingers and the accompanied complex patterns were recorded using a high-speed digital camera (Basler A2040-90um) coupled to computer for direct image acquisition and treatment. In addition, an ultra-high-speed camera (FASTCAM UX100) was occasionally used for extremely large flow velocities. The images were post-processed using MATLAB, ImageJ and the camera software. The inlet mean imposed velocity was determined by an Alicat mass flow controller with a resolution of 0.0001 lit/min.

2.1. Fluid preparation and characterization

Carbopol is widely used as a thickener in cosmetic and pharmaceutical products [35,38,68] and as a gelling agent in systems where clarity is needed. The Carbopol rheology is mainly controlled by the concentration and pH of the solution. Carbopol is initially mixed with water to create an acidic solution, which is then neutralized with a base agent at intermediate pH (e.g., NaOH).

Table 1

The ranges and values of the dimensional parameters in our work. The reported viscosity values correspond to the shear rates between 0.12 and 518 (1/s).

Parameter	Name	SI unit	Range or value
\hat{W}	Channel width	m	6.8×10^{-2}
\hat{w}	Finger width	m	$(5.6 - 23.2) \times 10^{-3}$
\hat{b}	Gap thickness	m	9×10^{-4} & 1.5×10^{-3}
\hat{L}	Channel length	m	2.6×10^{-1}
\hat{V}	Mean imposed flow velocity (flow rate divided by channel cross section)	m/s	$(0 - 307) \times 10^{-3}$
\hat{U}	Finger tip velocity	m/s	$(0 - 1705) \times 10^{-3}$
$\hat{\rho}$	Carbopol density	kg/m ³	$\sim 9.985 \times 10^2$
\hat{C}	Carbopol concentration	% (wt/wt)	$(1 - 1.5) \times 10^{-3}$
$\hat{\mu}$	Carbopol viscosity	Pa.s	$(5.2 - 793) \times 10^{-1}$
$\hat{\sigma}$	Surface tension	N/m	$\sim 6.6 \times 10^{-2}$
$\hat{\sigma}_{eff}$	Effective surface tension	N/m	$\sim (6.6 - 7.05) \times 10^{-2}$
$\hat{\tau}_Y$	Yield stress	Pa	5.5 – 13.7
\hat{N}_1	First normal stress difference	Pa	0 – 168.1
$\hat{\Lambda}$	Relaxation time	s	$\sim (0.4 - 134) \times 10^{-3}$
\hat{t}_{ave}	Wall residual layers average thickness	m	$(2.9 - 14.4) \times 10^{-5}$
\hat{n}_d	Number of cavities in the network structure regime	–	$(4.8 - 25.9) \times 10^1$
\hat{d}_{ave}	Mean characteristic diameter of cavities in the network structure regime	m	$(4.7 - 83) \times 10^{-4}$

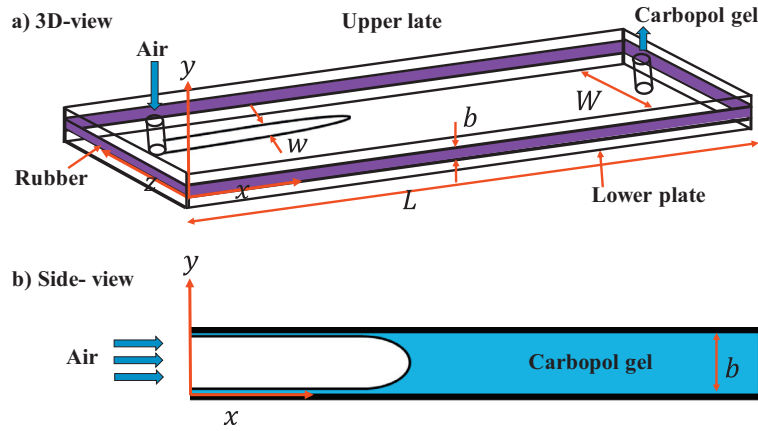


Fig. 1. Schematic view of the experimental set-up (i.e., a rectangular Hele-Shaw cell). a) A 3D-view of the geometry and the flow. b) Side view.

Table 2

The ranges and values of the dimensionless parameters in our work.

Parameter	Name	Definition	Range or value
Bn	Bingham number	$\frac{\hat{\tau}_Y}{\kappa(\hat{V}/\hat{b})^n}$	$(3 - 19) \times 10^{-1}$
Bn^*	Modified Bingham number	$\frac{Bn}{1+Bn}$	$(2 - 7.3) \times 10^{-1}$
Ca	Capillary number	$\frac{\hat{\mu}\hat{U}}{\hat{\sigma}_{eff}}$	$(9 - 146.5) \times 10^{-1}$
Ca^*	Modified capillary number	$\frac{Ca}{1+We^*We_c^*}$	$(5.9 - 120.5) \times 10^{-1}$
Re	Reynolds number	$\frac{\hat{\rho}\hat{U}\hat{b}}{\hat{\mu}}$	$(2.7 - 81000) \times 10^{-7}$
t	Relative film thickness	$\frac{\hat{t}_{ave}}{\hat{b}}$	$(34 - 96) \times 10^{-3}$
We	Weber number	$\frac{\hat{\rho}\hat{U}^2\hat{b}}{\hat{\sigma}_{eff}}$	$(6.5 - 789200) \times 10^{-5}$
We^*	Modified Weber number	$We \delta^{1+n}$	$(2 - 126200) \times 10^{-2}$
Wi	Weissenberg number	$\frac{\hat{\Lambda}\hat{U}}{\hat{b}}$	$(1.24 - 574) \times 10^{-2}$
δ	Aspect ratio	$\frac{\hat{W}}{\hat{b}}$	45.3 & 75.5
λ	Relative finger width	$\frac{\hat{w}}{\hat{W}}$	$(8 - 34) \times 10^{-2}$

At small concentrations, the density of the neutralized transparent solution is close to that of water.

For visualization purposes, the Carbopol gel used in our experiments was dyed with a small amount of black ink for visualization purposes. Three different Carbopol solutions were used for the experiments, for which the composition is shown in Table 3. The con-

ventional abbreviations introduced in the table for different Carbopol concentrations will be used throughout the rest of the paper. The rheological measurements for Carbopol solutions (termed low, medium and high concentrations) were performed using an AR-G2 TA Instrument digital controlled shear stress-shear rate rheometer. A cone-and-plate geometry was used, with 60 mm cone and plate diameter, 2.04° cone angle and 56 μm gap at the cone tip. Identical loading procedures were implemented in all tests.

Neglecting elastic effects and concentrating on viscoplastic properties, the Herschel–Bulkley model is an appropriate rheological model that describes the shear behavior of Carbopol gel:

$$\hat{\tau} = \hat{\tau}_Y + \hat{\kappa} \hat{\gamma}^n, \quad (3)$$

which also includes the simpler Bingham, power-law and Newtonian models. The Herschel–Bulkley model is defined by three parameters: a fluid consistency index ($\hat{\kappa}$), a yield stress ($\hat{\tau}_Y$), and a power-law index (n). The Herschel–Bulkley viscosity ($\hat{\mu}$), which depends on the Carbopol concentration and the shear rate (\hat{U}/\hat{b}), is calculated as (see Fig. 2a):

$$\hat{\mu} = \hat{\tau}_Y \left(\frac{\hat{b}}{\hat{U}} \right) + \hat{K} \left(\frac{\hat{U}}{\hat{b}} \right)^{n-1}. \quad (4)$$

Figure 2a shows that \hat{U}/\hat{b} affects the viscosity significantly, where the viscosity of Carbopol strongly decreases with the shear

Table 3

Carbopol composition and determined parameters from rheological measurements, assuming the Herschel–Bulkley model.

Carbopol solution	Carbopol % (wt/wt)	NaOH % (wt/wt)	$\hat{\tau}_Y$ (Pa)	$\hat{\kappa}$ (Pa.s ⁿ)	n
Low Carbopol concentration (LCC)	0.1	0.029	5.5	5.7	0.32
Medium Carbopol concentration (MCC)	0.12	0.035	8.3	7.6	0.31
High Carbopol concentration (HCC)	0.15	0.043	13.7	11.8	0.35

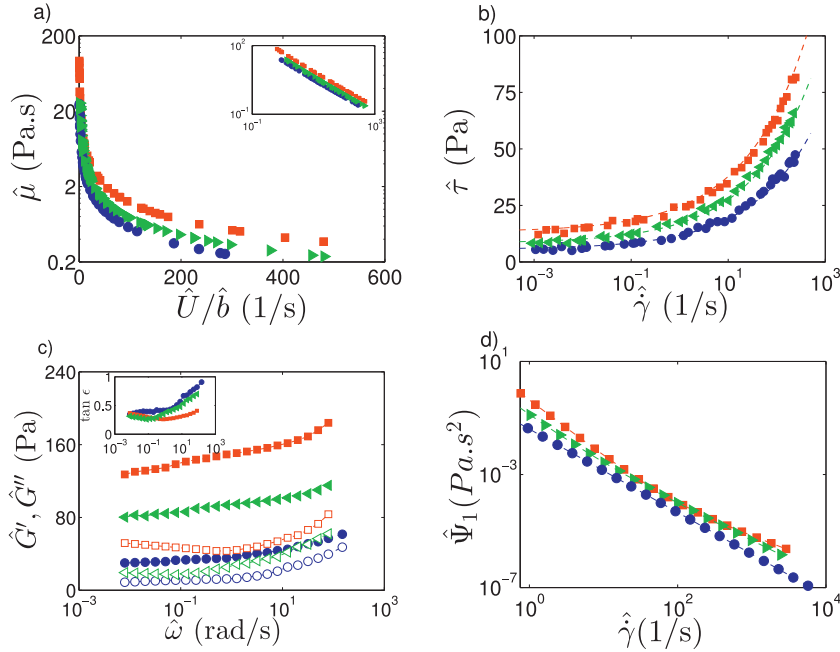


Fig. 2. Various rheology results for experiments with LCC (●), MCC (▲) and HCC (■). a) Viscosity ($\hat{\mu}$) as a function of the shear rate (\hat{U}/\hat{b}) based on Eq. (4). The inset shows the same data as in the main graph but with a logarithmic scale. b) Flow curves of the shear stress $\hat{\tau}$ versus the shear rate $\hat{\gamma}$. The dashed lines correspond to the Herschel–Bulkley model parameters fitted to data. c) The storage modulus (filled symbols) and the loss modulus (hollow symbols) as a function of frequency ($\hat{\omega}$). The inset shows the loss factor versus frequency. d) The first normal stress coefficient ($\hat{\Psi}_1$) as a function of the shear rate.

rate. Examples of rheometer flow curves of different Carbopol solutions (along with the fitted Herschel–Bulkley model data) are given in Fig. 2b. The yield stress value is enhanced by increasing the Carbopol concentration.

In order to gain insight about the elastic properties of our Carbopol gels, oscillatory frequency sweep tests (with the angular frequency $\hat{\omega}$) were conducted to quantify the relation between the elastic and viscous properties of the experimental samples. The values of the storage modulus, \hat{G}' (Pa), and that of the loss modulus, \hat{G}'' (Pa), depend on the Carbopol concentration of each sample. The storage and loss moduli represent elastic and viscous characteristics, respectively. Complex modulus can be calculated by $\hat{G}^* = \sqrt{\hat{G}'^2 + \hat{G}''^2}$. The loss factor, $\tan \epsilon$, is the ratio of viscous to elastic portion of the viscoelastic deformation, defined as $\tan \epsilon = \frac{\hat{G}''}{\hat{G}'}$. Figure 2c displays the variation of storage and loss moduli for different Carbopol gels. The values of both moduli increase with increments in the frequency. It can be also seen that by increasing the Carbopol concentration, the ratio of the storage modulus to the loss modulus is generally enhanced. The inset of Fig. 2c shows that the loss factor varies in the range of $0.3 \leq \tan \delta \leq 0.9$. Since the loss factor is smaller than unity, the elastic effects are important. Our Carbopol gels are generally comparable in their elastic behavior as well as loss factor with the values reported in the literature [18,35].

The Weissenberg number is the appropriate dimensionless number to quantify viscoelastic behaviors under flow, defined as

the ratio of the relaxation time ($\hat{\Lambda}$) to the timescale of flow (\hat{b}/\hat{U}). To find the Weissenberg number of our Carbopol gels, the following steps were taken. First, the first normal stress difference (N_1), as the evidence of elastic effects, was calculated using the Lodge–Meissner relation (which is frequently employed) [52]:

$$\hat{N}_1 = \gamma \cdot \hat{\tau}, \quad (5)$$

where γ and $\hat{\tau}$ are the shear strain and the shear stress, respectively. The former was calculated through amplitude sweep tests. It is accepted that the comparison between the calculated N_1 from the Lodge–Meissner relation and the values directly measured by a rheometer is satisfactory [52] and references therein). In the second step, the normal stress coefficient was found through its definition, i.e., $\hat{\Psi}_1 = \hat{N}_1/\hat{\gamma}^2$. Finally, $\hat{\Lambda}$ was determined by [19,87]

$$\hat{\Lambda} = \frac{\hat{\Psi}_1(\frac{\hat{U}}{\hat{b}})}{2\hat{\mu}(\frac{\hat{U}}{\hat{b}})}. \quad (6)$$

Figure 2d illustrates the first normal stress coefficient ($\hat{\Psi}_1$) as a function of the shear rate ($\hat{\gamma}$) for different Carbopol concentrations, showing that $\hat{\Psi}_1$ becomes trivial at larger shear rates and it increases with an increase in the Carbopol concentration.

We end this characterization section by reminding that the air–Carbopol surface tension value used for analyzing our experimental results is slightly lower than that of air–water, i.e., $\hat{\sigma} = 0.066$ (N/m), taken from the literature [8]. Through developing a Wilhelmy technique, Boujlel and Coussot [8] have shown that the

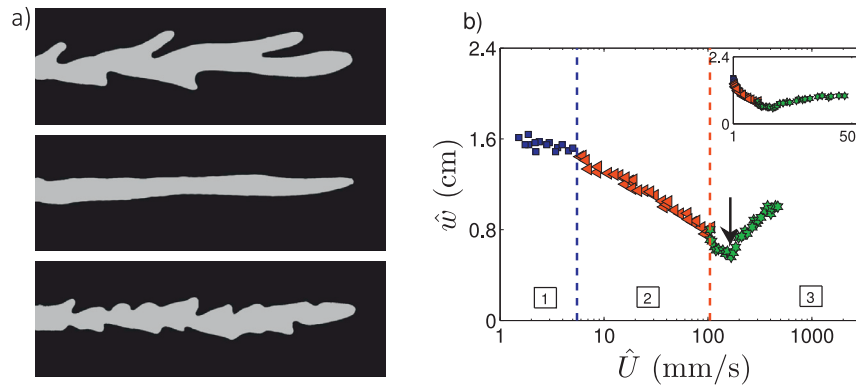


Fig. 3. Experimental results of the displacement of an MCC gel by air in a Hele-Shaw cell geometry with $\hat{b} = 0.9$ mm. a) Experimental images of the displacement flow. The air flows from left to right. Effects of increasing the mean imposed velocity (\hat{V}) on the finger patterns can be seen. The mean imposed velocities are $\hat{V} = 0.58, 6.3, 31.4$ mm/s and the finger tip velocities are $\hat{U} = 2.4, 30.2, 147.5$ mm/s, from top to bottom. The field of view for each of these snapshots is 4.7×21.3 cm². b) Variation of the finger width, \hat{w} , versus the finger tip velocity, \hat{U} . Three different flow regimes are marked by ■ (yield stress regime), ▲ (viscous regime), and ★ (elasto-inertial regime). The arrow indicates the transition point where inertial effects start to become important. The inset shows the same data as in the main graph but with a linear scale.

surface tension variation versus low concentrations of Carbopol is nearly negligible, which is the case in our experiments.

3. Results and discussions

In this section, we present and discuss our main findings for a wide range of experimental parameters studied. In a typical experiment, the cell is already full of Carbopol solution while a constant pressure gradient is applied to the system. Due the large viscosity difference between air and Carbopol, the air penetrates into the gel, forming various interesting patterns, which we will discuss below. Examining experimental results consists of two separate analyzes: first, analyzing the morphological behaviors based on experimental images and, second, quantifying the finger width and the finger tip velocity. The last two parameters remain almost constant throughout each experiment, except for close to the channel ends.

3.1. Main flow behaviors

Let us begin with explaining the main flow regimes in our experiments and their qualitative features. In a sequence of increasing the mean imposed displacement velocity, \hat{V} , while the rest of the flow parameters are fixed, we observe that the flow morphology changes significantly. For example, Fig. 3a presents three different regimes with distinct patterns observed in a typical experimental set. These flows regimes, also presented as videos in supplementary materials, can be explained as follows:

- At low \hat{V} , a *yield stress* regime is observed, which consists of many fingers (top image). In fact the process initially starts with a finger, for which the tip quickly splits and asymmetric fingers are formed. The destabilization and splitting continues and more fingers are progressively created. Therefore, the displacement flow eventually exhibits a ramified structure with many fingers.
- At larger \hat{V} , the flow behavior changes; here, a *viscous* regime with a single, narrow finger is found (middle image). The shape of this single finger is very similar to that of classical viscous fingers in Newtonian displacement flows [44,81]. In this regime, the tip splitting is suppressed. The formed finger is approximately symmetric and it is placed more or less in the middle of the channel.
- At much larger \hat{V} , the flow presents an *elasto-inertial* regime. In this pattern, there is usually an asymmetric finger in middle of the channel while there are secondary instabilities at the finger sides, leading to a side-branching structure (bottom image).

While the main finger does not present tip splitting, highly branched finger sides are eventually formed. These branches may have different lengths and angles. It may be worth noting the relevant literature of viscoelastic displacement flows where a variety of side branching morphologies, depending on the fluid type and the imposed velocity, are observed [49].

Although, these observations were described versus the mean imposed velocity \hat{V} , they can be equally presented versus the finger tip velocity (\hat{U}), since these two velocities are proportional. The finger tip velocity is however preferred as velocity scale to define the capillary number.

Figure 3d plots the variation of the finger width, \hat{w} , versus the finger tip velocity, \hat{U} . It should be noted that in some cases the local finger width varies along the channel so that the average finger width has been used to calculate all the dimensional and dimensionless parameters throughout this work. However, the variation of the local finger width with time is negligible. The three different flow regimes, which were explained in Fig. 3a, are marked by different symbols on this graph. At low \hat{U} , where the yield stress regime is found, the finger width remains nearly constant as \hat{U} increases. At larger \hat{U} , the finger width changes its behavior as it starts to continuously decrease with \hat{U} . At very large \hat{U} , the flow transitions to the elasto-inertial regime, where the variation of \hat{w} is not monotonic. For example, at the transition point to this regime, although the flow morphology changes, the finger width initially continues to decrease. However, at larger velocities, \hat{w} suddenly starts to increase and it finally reaches almost a plateau at extremely large \hat{U} (visible in the inset). The change in the morphology may be attributed to elastic effects, while the non-monotonic behaviors of \hat{w} implies the appearance of inertial effects. It will be argued later, in more details, that inertial effects are responsible for the increase in the finger width.

Figure 4 shows variation of the finger width versus the finger tip velocity, for different Carbopol concentrations and channel thicknesses. Although the value of \hat{w} is affected by both of these parameters, a general common behavior can be recognized for all experiments: \hat{w} is nearly independent of velocity at very small \hat{U} , decreases at medium \hat{U} , suddenly starts to increase at large \hat{U} and finally reaches almost a plateau at very large \hat{U} .

3.2. Yield stress regime

In an interesting experimental study using gels and foams, Lindner et al. [43,44] were first to quantify the yield stress regime of viscoplastic fluids. They backed up their experimental results with

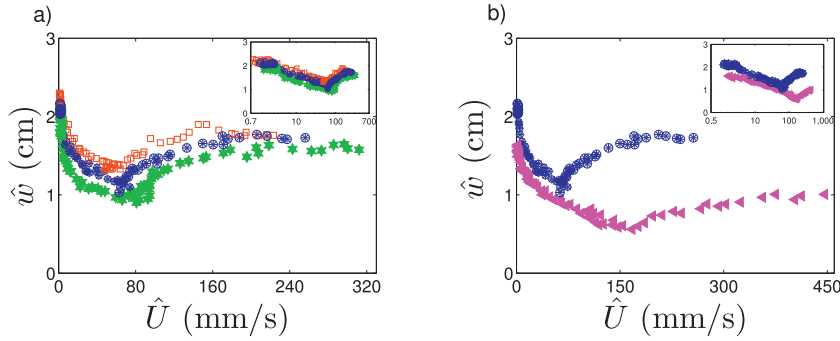


Fig. 4. Variation of the finger width versus the finger tip velocity: a) The results are shown for three Carbopol concentrations and a fixed channel thickness ($\hat{b} = 1.5$ mm). The data correspond to experiments with LCC (\square), MCC (\otimes) and HCC (\star). b) The results for two different channel thicknesses and a fixed MCC. The data correspond to experiments with $\hat{b} = 1.5$ mm (\otimes) and $\hat{b} = 0.9$ mm (\blacktriangleleft). The insets are the same as the main graph but with a semi-log x-axis, where the three regimes are more visible.

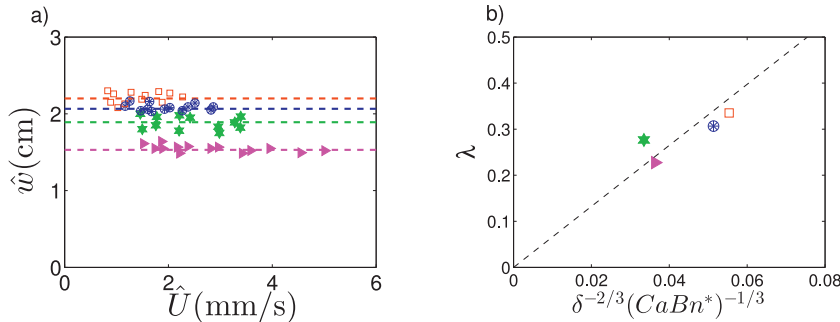


Fig. 5. Results for the yield stress regime with the following experimental parameters: $\hat{b} = 1.5$ mm & LCC (\square), $\hat{b} = 1.5$ mm & MCC (\otimes), $\hat{b} = 1.5$ mm & HCC (\star), and $\hat{b} = 0.9$ mm & MCC (\blacktriangleleft). (a) Variation of the finger width versus the finger tip velocity. The horizontal dashed lines show the mean values of \hat{w} for all \hat{U} in this regime. These mean values are used for plotting the subfigure on the right. (b) The dimensionless mean value of finger width ($\lambda = \hat{w}/\hat{W}$) as a function of $\delta^{-2/3}(CaBn^*)^{-1/3}$.

their theoretical predictions from an earlier paper [17]. Although our experimental gel is different, our results in this regime show very good agreement with the findings of Lindner et al. [43]; see also [46]. Although, Van dam et al. [81] have observed tip-splitting and ramified structure for the shear-thinning fluid at very low velocities, we believe that, similar to the work of Lindner et al. [43], the patterns observed in our experiments at low velocities are due to yield stress rather than shear-thinning effects. Figure 5 shows the finger width versus the finger tip velocity. As can be seen, there is not much noise in our experimental results, unlike those of Lindner et al. [43]. This figure shows that the finger width is independent of the finger tip velocity (or the mean imposed flow velocity) in the yield stress regime, for a large number of experimental data presented. The reason is that, for small \hat{U} , the yield stress is predominant so that the displaced fluid is not yielded everywhere and therefore the each air finger does not sense the presence of the channel walls or other fingers (see [43]). The appearance of the ramified structure can be attributed to this feature since the finger can frequently split without feeling the surroundings.

Based on Darcy's law, there is a linear relation between pressure gradient and velocity for Newtonian fluids in the Hele-Shaw cell. For these fluids, Chouki et al. [14] have demonstrated through linear stability analyzes that the wavelength of maximum growth ($\hat{\lambda}_m$) is governed by the ratio of capillary to viscous stresses expressed as $\hat{\lambda}_m \propto \sqrt{\frac{\hat{\sigma}\hat{b}^2}{\hat{\mu}\hat{U}}}$, in which the viscous stress has been approximated by $\frac{\hat{\mu}\hat{U}}{\hat{b}}$. However, the relation between pressure gradient and velocity for yield stress fluids is non-linear and instability may occur even at vanishing velocities [17]. Thus, as the stress approaches to the yield stress at low shear rates, we may simply replace the viscous stress in the relation for $\hat{\lambda}_m$ by the yield stress to

find $\hat{\lambda}_m \propto \sqrt{\frac{\hat{\sigma}\hat{b}}{\hat{\tau}_y}}$ [46]. More rigorously, Coussot [17] has analytically proved that this relation is appropriate. Assuming that the finger width after destabilization corresponds to the maximum growth wavelength, we can show that the dimensionless finger width in the yield stress regime satisfies $\lambda \propto \delta^{-2/3}(CaBn^*)^{-1/3}$, where Bn^* is the modified Bingham number [78] defined as $Bn^* = \frac{\hat{\tau}_y}{\hat{\tau}_{y+\kappa}(\hat{V}/\hat{b})^n} = \frac{Bn}{1+Bn}$. Figure 5b shows the dimensionless mean value of the finger width λ as a function of $\delta^{-2/3}(CaBn^*)^{-1/3}$, showing a nearly-linear relation, which is in good agreement with previous theoretical [17] and experimental observations for other types viscoplastic fluids [43,46].

3.3. Viscous regime

We showed earlier that at higher velocities, the displacement of Carbopol by air transitions from the yield stress regime to the viscous regime. Two features are associated to the viscous regime in our viscoplastic displacements. First, morphologically, a thin finger advances in the middle of the channel. Second, the finger width decreases as the mean imposed flow velocity or the finger tip velocity increases. Let us look further into the variation of the finger width in this regime.

Figure 6a presents the variation of the dimensional finger width (\hat{w}) as a function of the finger tip velocity (\hat{U}) for various experimental parameters. All of the experimental data show a continuous decrease in \hat{w} in the viscous regime. In this regime, viscous forces balance surface tension forces. The latter increase as the velocities increase. Figure 6a interestingly shows that for a given \hat{U} , the width of finger decreases by increasing the concentration of Carbopol, which is perhaps due to the overall increase in the vis-

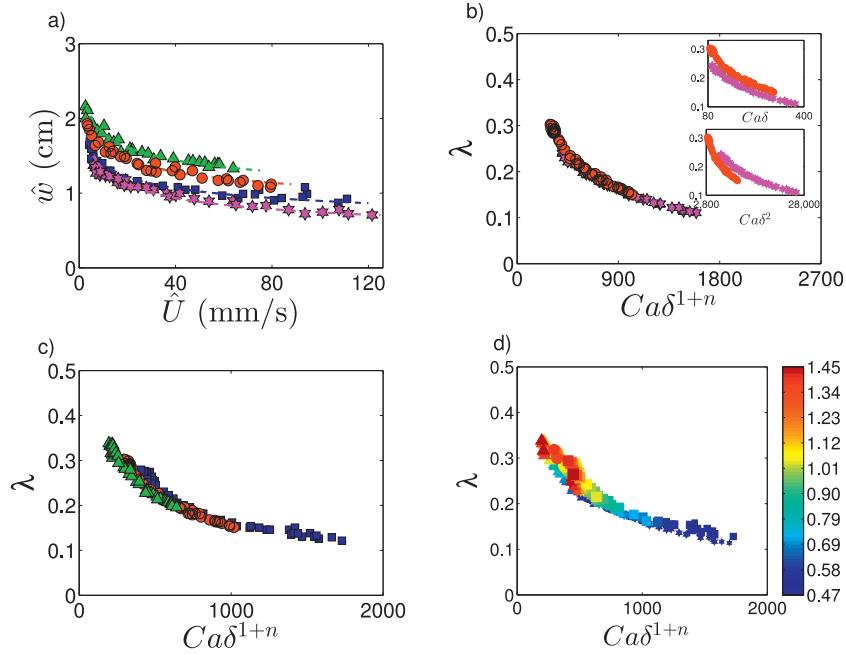


Fig. 6. Finger width versus various parameters for $\hat{b} = 1.5$ mm & LCC (\blacktriangle), $\hat{b} = 1.5$ mm & MCC (\bullet), $\hat{b} = 1.5$ mm & HCC (\blacksquare), and $\hat{b} = 0.9$ mm & MCC (\blacklozenge). a) \hat{w} versus \hat{U} . The dashed lines are fitted curves as eye guides. b) λ versus $Ca \delta^{1+n}$, showing the collapse of two data sets (different channel thicknesses) onto a single curve. In the top & bottom insets, the exponents of δ are 1 and 2, respectively. c) λ as a function $Ca \delta^{1+n}$, showing the collapse of 4 data sets (different Carpool concentrations) onto a single curve. d) Values of the Bingham number Bn (indicated by size and by the color in the color bars), plotted against λ and $Ca \delta^{1+n}$ for all the data sets. (For interpretation of the references to color in this figure legend, the reader is referred to the web version of this article.)

cosity of the Carbopol solution. In addition, this subfigure shows that for a constant Carbopol concentration, increasing the channel thickness widens the displacement flow finger.

It is known that for Newtonian fluids, $Ca \delta^2$ is the appropriate dimensionless group which enables the collapse of all finger widths onto a master curve [30,50,75,80]. This dimensionless group has been also used for weakly shear-thinning fluids with modified Darcy’s law in which viscosity $\hat{\mu}$ is substituted by shear dependent viscosity $\hat{\mu}(\hat{\gamma})$ [3,36,41,65,80]. Lindner et al. [41] showed that this substitution is only valid when the fluids are very weakly shear-thinning ($n > 0.65$). This becomes relevant to our work since the power-law index in the Herschel–Bulkley model (n) for our gel is less than 0.4 so that our fluids are not weakly shear-thinning. Lindner et al. [43] suggested $Ca \delta$ as a suitable dimensionless group for viscoplastic fluids with significant shear-thinning effects. Figure 6b plots λ versus $Ca \delta^{1+n}$ while the insets are versus $Ca \delta^2$ and $Ca \delta$. We observe from the insets that neither $Ca \delta^2$ nor $Ca \delta$ enables a perfect collapse of the data. Instead, as the results of the main figure suggest, $Ca \delta^{1+n}$ works nearly perfectly as the control parameter for our experiments. The exponent of the aspect ratio that we propose ($1+n$) shows that the dependency on the aspect ratio is weaker compared to Newtonian fluids, which may be attributed to 3D effects [43]. The exponent seems valid for our moderately shear-thinning viscoplastic fluids while it is also consistent with previous finding for Newtonian fluids ($n = 1$) as well as strongly shear-thinning fluids ($n \ll 1$). Although our results seem reasonable, the mechanism behind the modification of the dimensionless group is not crystal clear. In addition to 3D effects, the literature also suggests that the deviation from Darcy’s law for strongly shear-thinning fluids may be due to slip layers formation for these fluids in the flow [36,37]. These layers in polymeric liquids originate from velocity gradient at the solid-liquid interface at high shear rates [36,48,53].

Figure 6c shows a reasonable collapse of λ versus $Ca \delta^{1+n}$, for various Carbopol concentrations. Figure 6d plots a neat collapse of data for all sets of experiments in the viscous regime. The values of

the Bingham number are superposed as color bars onto this figure, showing the true nature of viscous domination: the data points clearly have different Bn but they nevertheless collapse onto the same master curve. Generally, it is clear from this subfigure that the capillary and Bingham numbers have opposite effects on the dimensionless finger width, λ : by increasing Ca the finger width decreases but by increasing Bn generally (not always) the finger width increases.

3.4. Transition between viscous and yield stress regimes

One would like to ideally distinguish different flow regimes versus the dimensionless groups that govern the flow. It is *a priori* expected that Ca must be an important parameter to govern the transition between the viscous and yield stress regimes. In addition, a suitable dimensionless number to consider yield stress effects is the Bingham number. To find the appropriate dimensionless group governing the transition, various combination of the dimensionless forms were examined. Figure 7a shows the variation of λ versus $Ca \delta^{1+n}/Bn$ for the yield stress and the viscous regimes. For different experimental parameters, it can be seen that λ is initially independent of $Ca \delta^{1+n}/Bn$ whereas it decreases versus $Ca \delta^{1+n}/Bn$ after a transition point, which takes place at $Ca \delta^{1+n}/Bn \approx 550$, on average. Figure 7b shows the experimental data points that belong to different flow regimes in the plane of $Ca \delta^{1+n}$ and Bn . The yield stress, viscous and elasto-inertial regimes are marked by different symbols. An oblique dashed line is superposed on this figure and it has a slope of $Ca \delta^{1+n}/Bn = 550$ (based on the findings of Fig. 7a), which can interestingly separate the yield stress and viscous regimes. The special form of the transition dimensionless group, i.e., $Ca \delta^{1+n}/Bn$, may be justified by reminding that the transition between the yield stress and viscous regimes occurs at a critical point where the ratio of viscous to surface tension stresses (Ca) significantly exceeds that of yield to viscous stresses (Bn).

To test accuracy of $Ca \delta^{1+n}/Bn \approx 550$ to delineate the transition between the yield stress and viscous regimes, several data

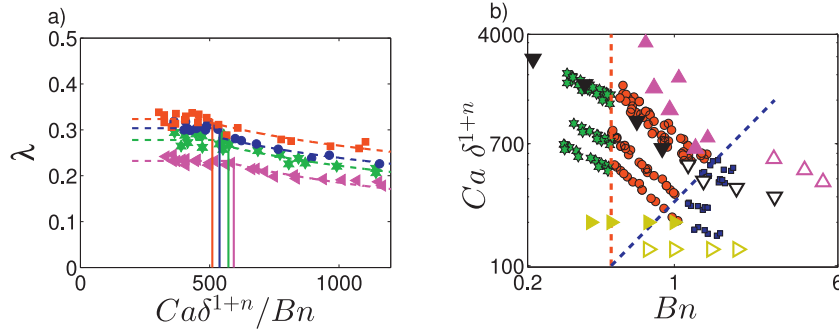


Fig. 7. a) λ as a function of $Ca \delta^{1+n} / Bn$. The dashed lines are fitted curves as eye guides. The vertical solid lines indicate the transition points at which λ starts to decrease, for each experimental sequence of increasing velocity (on average $Ca \delta^{1+n} / Bn \approx 550$). The data correspond to the experiments with $\hat{b} = 1.5$ mm & LCC (■), $\hat{b} = 1.5$ mm & MCC (●), $\hat{b} = 1.5$ mm & HCC (★), and $\hat{b} = 0.9$ mm & MCC (◀). b) Different flow regimes observed in the plane of $Ca \delta^{1+n}$ and Bn . The symbols correspond to the yield stress regime (■), the viscous regime (●), and the elasto-inertial regime (★). The oblique dashed line indicates the transition between the yield stress and viscous regimes ($Ca \delta^{1+n} / Bn = 550$). The vertical dashed line at $Bn = 0.5$ separates the data corresponding to the viscous and elasto-inertial regimes. The yield stress and viscous regime data points from the literature are also superposed. The symbols correspond to the yield stress regime (hollow symbols) and the viscous regime (filled symbols). The data are from [43] (▼, ▽), [21] (▶, ►) and [46] (▲, △).

points from different experimental and numerical studies available in the literature [21,43,46] are also superposed on Fig. 7b. This figure shows that proposed relation is more or less in good agreement with the previous findings from diverse studies.

In Fig. 7b, the data points corresponding to the viscous and elasto-inertial regimes are also segregated, on the two sides of the vertical dashed line at $Bn \approx 0.5$. This implies that the transition to elasto-inertial regime occurs when the yield stress effects, captured by the Bingham number, are negligible ($Bn < 0.5$). However, we have already shown that small Bn flows for our Carbopol solutions correspond to large Wi flows. In fact, as will be shown in the following section, although Fig. 7b shows the smallness of the relative yield stress effects in the elasto-inertial regime, the critical transition between the viscous and elasto-inertial regimes is in fact govern by Wi not Bn .

3.5. Elasto-inertial regime

By increasing the mean imposed flow velocity, we transition from the viscous regime to the elasto-inertial regime. By “elasto-inertial” regime, we mean a regime where both elastic and inertial effects are present. Morphologically, in this regime, there usually exists a single finger in more or less the middle of channel while the sides of the finger present branches or wavy-like interfacial patterns. This is attributed to elastic effects (creating non-zero first normal stress difference). In terms of the finger width in this regime, \hat{w} initially continues to decrease with \hat{U} but suddenly starts to increase at a critical \hat{U} . This feature seems to be due to non-negligible inertial effects [12].

In terms of the finger width, another aspect is also observed, i.e., \hat{w} eventually reaches almost a plateau value, which we will discuss first in this section. Figure 8a shows the variation of \hat{w} with \hat{U} for different Carbopol concentrations and channel thicknesses, for the data points belonging to the elasto-inertial regime. Although the results differ from one another, one trend seems common: after the initial increase, all the curves seem to reach more or less plateau values. However, the plateau finger width for our fluid is significantly narrower than the classical plateau value of Newtonian fluids. For example, for the high Carbopol concentration and the fixed channel thickness $\hat{b} = 1.5$ mm, the dimensionless finger width reaches $\lambda \approx 0.24$, compared to $\lambda \approx 0.5$ reported for Newtonian fluids. One hypothesis to justify this discrepancy is that interfacial patterns may be modified due to anisotropy [4,16,67,88] near the finger, resulting in reduced plateau values. This has been examined through using a thin wire inside the Hele-Shaw cell [67,88], having a small bubble on the finger tip [16,67], and grooving in the

top/bottom plates of the channel [67]. An anisotropy state may also exist as a result of the shear dependent viscosity in non-Newtonian fluids, which has been confirmed numerically [24,37]. For example, the plateau value of λ for shear-thinning fluids at higher finger tip velocities is less than 0.5 because of the smaller viscosity value at the interface, which has been reported experimentally [42].

Figure 8b interestingly shows that the curves can be superposed provided that $1/\lambda \delta^{1+n}$ is used as the dimensionless group, in which viscous effects are apparently absent. This dimensionless group shows that the finger width selection mechanism is completely different from that for Newtonian fluids, although we are unable to fully justify why $1/\lambda \delta^{1+n}$ enables the collapse of data.

3.5.1. Inertial effects

Let us attempt to quantify inertial effects and their role in the transition point where the width of the finger starts to increase. The relevant dimensionless number for this purpose is the Weber number defined as $We = \frac{\hat{\rho} \hat{U}^2 \hat{b}}{\hat{\sigma}_{eff}}$, where $\hat{\rho}$ is the density of the Carbopol gel and $\hat{\sigma}_{eff}$ is the effective surface tension. At high shear rates (elasto-inertial regime) the effective surface tension ($\hat{\sigma}_{eff}$) is more relevant than the surface tension ($\hat{\sigma}$) since the normal stress exerts extra stress on the finger, which should be taken into account. The effective surface tension is calculated through [42]:

$$\hat{\sigma}_{eff} = \hat{\sigma} + 1/2 \hat{N}_1 (\hat{\gamma}) \hat{b}. \quad (9)$$

The Weber number quantifies the importance of inertial to surface tension stresses. Our investigation shows that the transition to inertial effects is governed by a modified Weber number (We^*) defined as:

$$We^* = We \delta^{1+n}. \quad (8)$$

Figure 9a shows that by increasing the modified Weber number, λ starts to increase at a critical modified Weber number of $We^*_c \approx 76.5$ for all the experiments performed at different experimental conditions. Regarding the finger width for Newtonian fluids, it has been shown that the dimensionless group $Ca \delta^2$ can be modified to include inertial effects [12]. Based on this idea, for our non-Newtonian fluid we propose a modified capillary number as a new dimensionless group to help collapse the λ data that belong to viscous and elasto-inertial regimes on the same graph:

$$Ca^* = \frac{Ca \delta^{1+n}}{1 + We^*/We^*_c}. \quad (9)$$

It can be concluded from Eq. (9) that when We^* is small, $Ca^* \rightarrow Ca \delta^{1+n}$, and when We^* is very large, $Ca^* \rightarrow \frac{We^*_c}{Re}$ (where $Re = \frac{\hat{\rho} \hat{U} \hat{b}}{\mu}$),

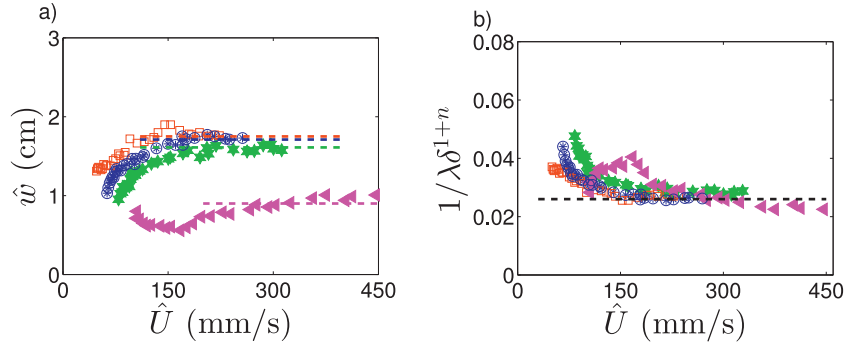


Fig. 8. Results for the elasto-inertial regime with the following experimental parameters: $\hat{b} = 1.5$ mm & LCC (\square), $\hat{b} = 1.5$ mm & MCC (\otimes), $\hat{b} = 1.5$ mm & HCC (\blacklozenge), and $\hat{b} = 0.9$ mm & MCC (\blacktriangleleft). a) The finger width as a function of the finger tip velocity. b) Superposition of the experimental data when $1/\lambda\delta^{1+n}$ is used. The dashed line shows a plateau value of $1/\lambda\delta^{1+n} = 0.026$.

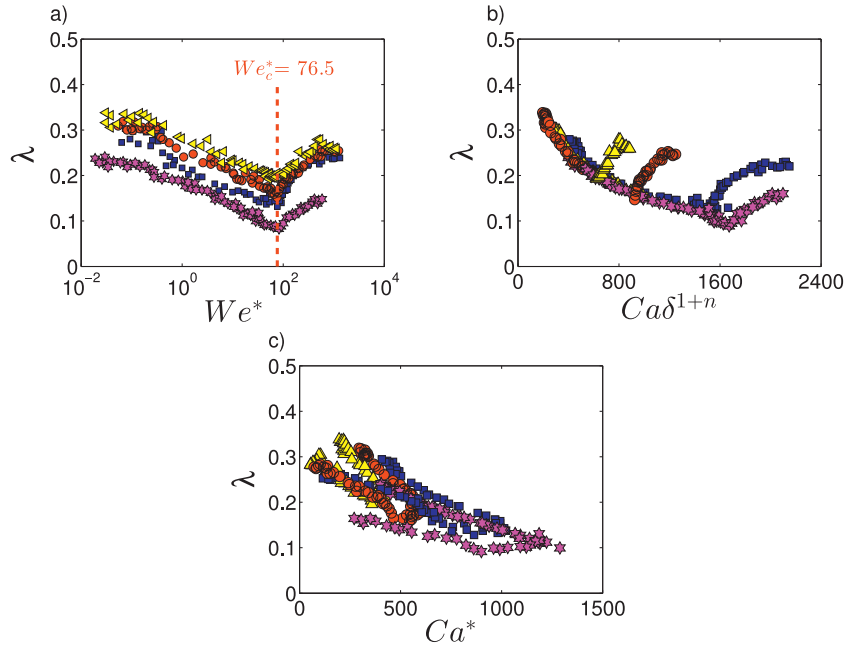


Fig. 9. The dimensionless finger width as a function different dimensionless groups for data at different aspect ratios and Carpool concentrations: a) λ as a function We^* . b) λ as a function $Ca \delta^{1+n}$. c) λ as a function Ca^* . The data correspond to experiments with $\hat{b} = 1.5$ mm & LCC (\blacktriangle), $\hat{b} = 1.5$ mm & MCC (\bullet), $\hat{b} = 1.5$ mm & HCC (\blacksquare) and $\hat{b} = 0.9$ mm & MCC (\blackstar).

both of which seem to be reasonable limits. Furthermore, the Reynolds number varies in the range of $(2.7 - 81000) \times 10^{-7}$. Note that to calculate the capillary number (Ca), we have used the effective surface tension ($\hat{\sigma}_{eff}$), which is equal to $\hat{\sigma}$ for the yield stress and viscous regimes.

While Fig. 9b shows that λ corresponding to the experimental data points including viscous and inertial flows do not collapse versus $Ca \delta^{1+n}$, Fig. 9c shows that a good improvement with respect to the collapse of a wide range of experimental data can be achieved when Ca^* is used as the dimensionless group. However, the collapse onto a single curve is not perfect. One reason for the discrepancy might be that three-dimensional effects due to inertia have been ignored, while it is known such system can be considered two-dimensional when the inertia effects are negligible [69]. Another reason may be related to the (non-uniform) thickness of the wetting film of the displaced non-Newtonian fluid, which was not taken into account in our analyzes.

3.5.2. Elastic effects

We have already shown that the Carpool gel that we are using has elastic properties manifested at very large shear rates, cap-

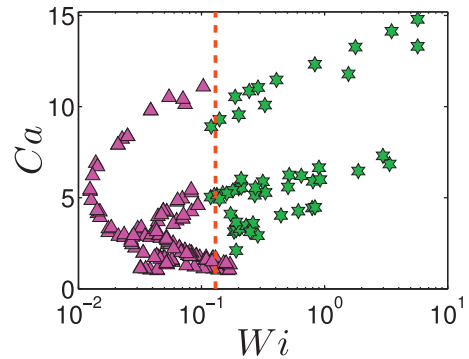


Fig. 10. The regimes classification based on elastic properties. Viscoelastic regime (\blackstar) and inelastic regime (\blacktriangle). The vertical dashed line shows $Wi = 0.13$, which is roughly the transition to elasto-inertial regime.

tured by the relevant dimensionless number, i.e., the Weissenberg number (Wi). Figure 10 classifies the experimental data points that belong to the elasto-inertial regime and those that do not, in the plane of Ca and Wi . It is seen that the data points of the elasto-inertial regime are clearly segregated as they are located at the

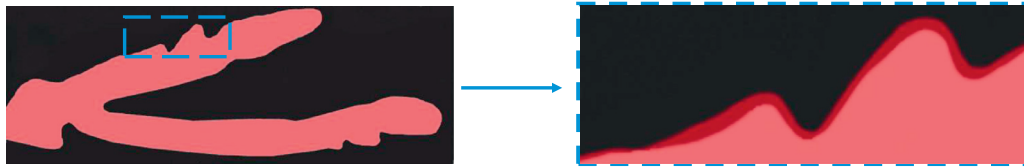


Fig. 11. An experimental snapshot showing the movement of the finger side due to an elastic response. The right image is zoomed-in on the indicated box of the left image. The red color indicates the displacing fluid (air) and the black color shows the displaced fluid (Carbopol). The dark red color shows the oscillation of the Carbopol layer within $\hat{t} = 0.358 - 0.4$ (ms). The images show the field of view of 5.8×17.5 cm² (left) and of 4.3×1.25 cm² (right). (For interpretation of the references to color in this figure legend, the reader is referred to the web version of this article.)

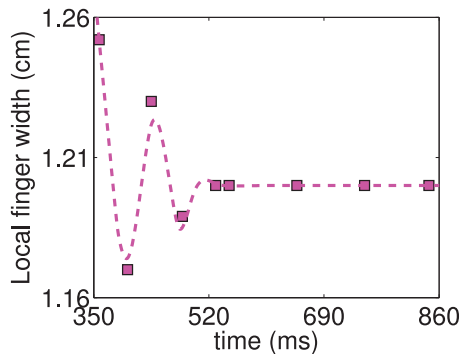


Fig. 12. The oscillation in the local finger width due to elastic response at different times with respect to the beginning of the experiment. The dashed line is smoothing spline fitted curve.

higher Wi end. The transition to the elasto-inertial regime (with side-branching features) seems to be occurring at more or less $Wi \approx 0.13$, although a small dependency on Ca may be also recognized on the graph. At small Wi , the inelastic data points include both the yield stress regime (with a ramified structure) and the viscous regime (with a narrow single-finger).

For shear-thinning fluids, Kondic et al. [37] reported that at higher velocities the growth of shorter wavelengths is increased; consequently, more side branches are created. We have observed a similar feature for our visco-elasto-plastic fluid at larger shear rates. Loosely speaking, elasticity in elasto-inertial regime creates extra stresses in the finger sides (due to the first normal stress difference) that lets (shortwave) perturbations grow, leading to side branching patterns. Therefore, in this regime, the evolution of finger patterns is controlled by a competition between viscous and elastic forces.

Although we have so far observed the “indirect” influence of elasticity through changing the first normal stress difference (allowing for perturbations to grow), we expect major detectable elastic response to be only seen at extremely high shear rates, with significantly larger Wi . Unlike the flows at $Wi \sim O(1)$ where the deformations are observed to be totally irreversible, for larger Wi , we may expect to detect a real elastic response (which is at least partially reversible). Therefore, we set up an experiment at an extremely large finger tip velocity (i.e., 2000 mm/s), which corresponds to $Wi = 5.74$ and $\hat{\Lambda} = 18.7$ (ms) (i.e., the relaxation time). The ultra-high-speed camera was set to take 2000 images per second. Figure 11 depicts an experimental image which shows the elastic response of our gel. We observe that the side branches move back and forth when undergoing large stresses due to the extremely rapid air flow.

Figure 12 shows that the variation of the local finger width versus time for the experiment of Fig. 11. Two effects can be seen: first, it is observed that the local finger width initially oscillates but it relaxes shortly after a few oscillations. Second, the deforma-

tion is not totally reversible, due to viscous dissipation. This experiment is also interesting in providing valuable information. For example, lengthwise, it can be seen that the maximum deviation is 6.4% compared to initial finger width. With regard to time, the time corresponding to the maximum deviation of the finger width is $\Delta \hat{t}_m \approx 42$ (ms) and the time needed for the finger to completely relax is $\Delta \hat{t}_m \approx 139$ (ms). The latter is interestingly in the order of the longest relaxation time.

4. Secondary features of the displacement flow

It must be accepted that the flow that we consider present various, complex features and we cannot cover all the flow aspects in a single study. However, there are secondary features of the displacement flow that are worth discussing in the present work. In this section, we attempt to introduce and explain two of these interesting features in the following two subsections below.

4.1. Static residual wall layers

The first secondary feature of the flow that we look into is related to the flow in the cross section of the channel. Through a comparison between the flow volume measured by the flow meter and that calculated through image processing, we have found out that the Carbopol gel cannot be completely swept out by the air within the cross section of the channel. This implies the existence of wetting films of Carbopol adjacent to the lower and the upper plates of the Hele-Shaw cell. Assuming a zero film thickness, image processing can deliver a mean imposed flow velocity, \hat{V}_M , which can be compared to the real mean imposed flow velocity, \hat{V} , measured by the flow meter. These two velocities can be simply related through

$$\frac{\hat{V}_M}{\hat{V}} = \frac{\hat{b} - 2\hat{t}_{ave}}{\hat{b}}, \quad (10)$$

where \hat{t}_{ave} is the mean wall film thickness defined as $\hat{t}_{ave} = \frac{\hat{t}_u + \hat{t}_l}{2}$ with \hat{t}_u and \hat{t}_l being the wetting layer thicknesses in the upper and lower walls, respectively.

Figure 13a shows the dimensionless mean thickness of the wetting films ($t = \frac{\hat{t}_{ave}}{\hat{b}}$) versus the capillary number. It can be seen that by increasing the capillary number, t increases, which seems to be a reasonable effect: as the relative surface tension stress decreases the film layer thickness increases. At larger Ca (~ 10), it can be observed that the mean film thickness in the vicinity of the wall can reach up to %10 of the gap thickness while Tabeling & Libchaber [75] observed that the mean residual layer thickness for Newtonian fluids reached up to %1 of the gap thickness at small capillary number ($Ca < 5 \times 10^{-3}$). In this work, due to dealing with large capillary numbers in the presence of a yield stress (proportional to the Carbopol concentration), the wetting layer thickness is relatively large. Thus, expectedly our results do not follow the Bretherton’s law, which is only applicable to Newtonian fluids in

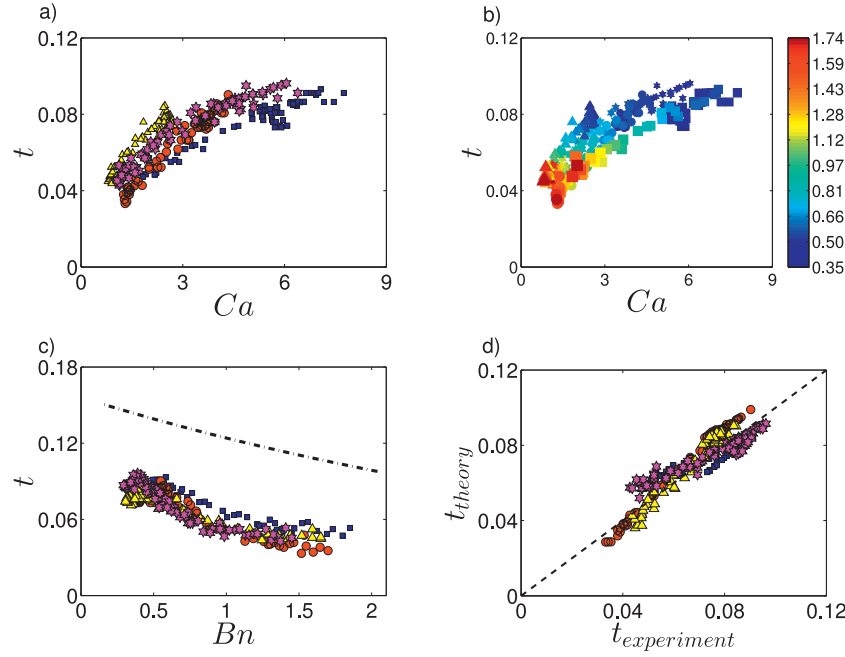


Fig. 13. Results for experimental data corresponding to $\hat{b} = 1.5$ mm & LCC (\blacktriangleright), $\hat{b} = 1.5$ mm & MCC (\bullet), $\hat{b} = 1.5$ mm and HCC (\blacksquare), and $\hat{b} = 0.9$ mm & MCC (\blackstar). a) Thickness of wetting film (t) as a function of Ca . b) Variation of Bn in the plane of t and Ca . The colors/symbol sizes illustrate the magnitude of Bn . c) Variation of t versus Bn . The dash-dot line shows h_{circ} from Eq. (11), i.e., when $Ca \rightarrow \infty$. d) Comparison between the experimental and theoretical prediction (Eq. (14)) of the wall layer thickness. The dashed line shows $t_{experiment} = t_{theory}$. (For interpretation of the references to color in this figure legend, the reader is referred to the web version of this article.)

small capillary numbers and breaks down for large values of capillary numbers ($Ca > 10^{-2}$) [76].

Figure 13b shows the same data points as in Fig. 13a while the values of Bn are marked by colors and symbol sizes. This figure shows that increasing Bn generally results in decreasing t , which may seem counter-intuitive at a first glance. In fact, increasing Bn of the displaced fluid influences the plug ahead of the displacing finger and results in a reduction of the residual wall layer thickness [84]. It should be noted that, for the ranges of the dimensionless numbers studied, the maximum variation of the film thickness with respect to the mean value is ± 0.048 mm and the variation of finger width is $\approx \pm 7.1$ mm. Therefore, the variation of film thickness does not have a significant effect on the finger.

After displacing finger tip has passed, the residual wall layers in our experiments do not seem to move; thus, it may be reasonable to assume that they are completely static. For miscible displacement flows at their immiscible limit (i.e., $Ca \rightarrow \infty$), static residual wall layers of viscoplastic fluids have been first analyzed by Allouche et al. [2]. Their combined theoretical and computational study for symmetric 2D channel flows showed that the wall layer thickness can be well approximated by the recirculation layer thickness, h_{circ} , defined as a thickness at which a steadily displacing finger would advance with the same velocity as that of the center-line of the downstream flow. Provided that $t < h_{circ}$ a recirculatory region would occur in the channel center, in front of the displacing finger within the cross section, which in return increases viscous dissipation. The flow prefers to avoid this situation. h_{circ} depends only on the Bingham number and it is defined as [2,84]:

$$h_{circ} = 1 - \frac{2Y}{Bn(1-Y)^2}, \quad (11)$$

where Y is found through the solution of

$$Y^3 - 3Y \left[1 + \frac{2}{Bn} \right] + 2 = 0, \quad (12)$$

for a given Bn . The residual wall layer thickness in the theory above shows an inverse relation to Bn , which is consistent with our experimental observations. In a recent computational study for channel flows, Swain et al. [74] have also showed that at low Bingham number ($Bn < 30$), increasing the Bingham number leads to decreasing the average residual layer thickness.

Using Eq. (11), h_{circ} has been calculated and superposed as a dash-dot line on Fig. 13c. The data points on this figure show the mean wetting layer thickness versus Bn . Although the trend is reasonable, h_{circ} overestimates the static wall layer thickness in our experiments, which is due to the presence of the non-negligible surface tension stress in our flows; in other words $Ca \sim O(1)$ in our experiments. In general $t = f(Bn, 1/Ca)$ and one may assume that $f(Bn, 0) = h_{circ}$. When $Ca \neq \infty$, using Taylor series, we can therefore write

$$t = f\left(Bn, \frac{1}{Ca}\right) = f(Bn, 0) + f'(Bn, 0) \frac{1}{Ca} + \frac{f''(Bn, 0)}{2} \frac{1}{Ca^2} + \frac{f'''(Bn, 0)}{6} \frac{1}{Ca^3} + \dots, \quad (13)$$

for which the best fit from the experimental results furnishes

$$t \approx h_{circ} - \frac{0.024}{Ca} + \frac{0.098}{Ca^2} - \frac{0.126}{Ca^3}. \quad (14)$$

To test the accuracy of modified theoretical equation above, the predicted layer thicknesses using Eq. (14) versus the experimental layer thicknesses reported in Fig. 13c are presented in a parity plot, illustrated in Fig. 13d. This figure shows the modified equation is fairly successfully to predict the wall layer thickness, for a wide range of experiments at different values of Ca and Bn .

4.2. Network structure regime

One of the interesting features observed in some of our experiments was a secondary flow aspect, which we term a *network structure* regime, associated to the formation of Carbopol network structures within the finger domain, after the displacing front

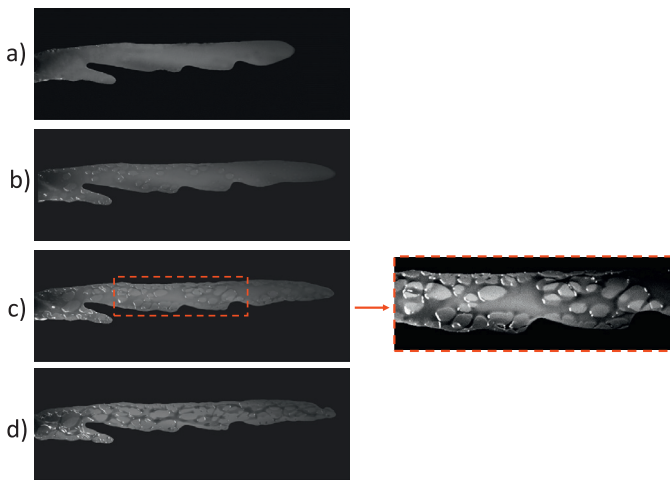


Fig. 14. An experimental snapshot (top view) showing 4 sequential steps of the process of the network structure formation within the finger domain. The experimental times are 1326, 1353, 1393, 1473 (ms), from top to bottom. The mean imposed velocity is $\bar{V} = 34.6$ mm/s (the finger tip velocity is $\bar{U} = 315.3$ mm/s). The images correspond to the experiment with $\bar{b} = 0.9$ mm & LCC. The field of view for these snapshot is 22.8×5.6 cm².

had already passed. This effect was seen in the experiments conducted at lower concentrations of Carbopol and very high mean imposed velocities. In order to simplify the explanation of the network structure regime, we divide the process into 4 main stages, i.e., the thin residual layers formation (stage 1), the residual layers break up and formation of cavities (stage 2), the extension of cavity area (stage 3), and the final structure formation (stage 4).

We now try to explain the 4-stage process step by step using Fig. 14, illustrating 4 sequential images (top view of the cell), for an experiment conducted with LCC at a large imposed air flow rate. These images were taken at 90 (fps). The first stage of the process, i.e., the formation of the thin residual layers, is straightforward. As the air displaces the Carbopol gel, a finger is formed. Within the channel cross section, as the finger tip advances, two thin residual layers of the Carbopol gel are left behind on the upper/lower walls of channel. These residual layers within the finger domain can be distinguished by the gray color area in Fig. 14a (which means that in this area, both air and Carbopol are present). In this first stage, nothing in particular is observed inside the finger. After a few microseconds, as seen in Fig. 14b, a partial break up of the residual Carbopol layers is observed, which is perhaps one of the reason to form some cavities (i.e., stage 2). In the stage of the extension of cavity area (i.e., stage 3), in Fig. 14c, the break up of the residual layer continues and the area of cavities is increased. The extension stage continues until the thickness of the residual layer becomes constant and the final structure formation stage is reached (Fig. 14d). At this stage, a network of Carbopol structure is formed inside the finger domain.

A schematic view of what we think is happening may be helpful. Figure 15a shows a schematic (cell side view) of the 4 sequential stages observed in the network structure regime. The top image is the formation of the thin residual layers of Carbopol gel, adjacent to the walls. In the second stage, the residual layers are broken perhaps since the wall shear stress overcomes the bonding strength in the Carbopol gel layers, causing the cavities to form. In the third stage, the remaining Carbopol pieces on the walls retract and the cavity area extends. Finally, in the final stage, i.e., the structure formation, the residual pieces are almost stationary (and the thickness of Carbopol pieces remains constant).

It seems that the residual layers break up is a key stage in the network structure regime. Two aspects may be important: non-

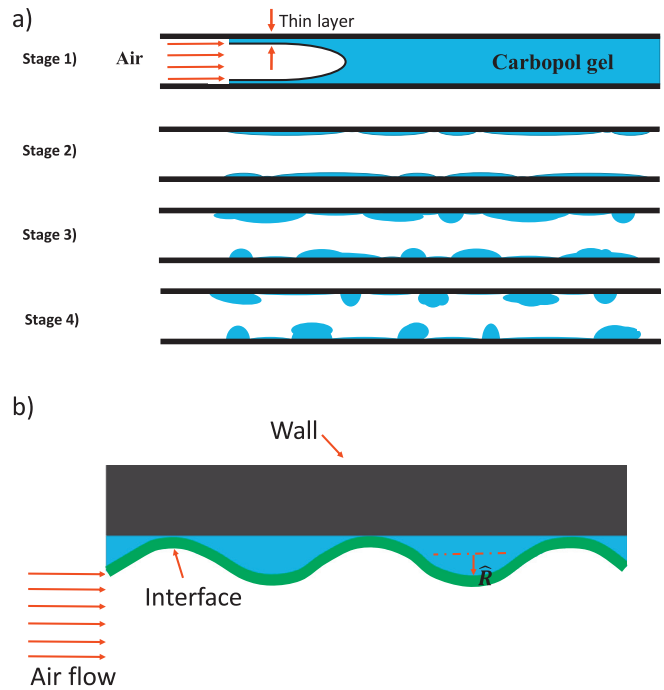


Fig. 15. a) Schematic of a probable 4-stage process of the formation of network structure regime (side channel view). b) Schematic of the intermediate stage of the network structure formation, as the residual layer breaks up into several pieces.

uniformity of the residual layer and the bonding strength of Carbopol. Regarding the latter aspect, at low Carbopol concentrations, the large wall shear stresses induced by the air flow overcome the Carbopol bonding strength so that they are able to significantly weaken the structure of the residual film. Afterwards, the former aspect becomes important: due to the layer non-uniformity, the thin layer is vulnerable to instabilities caused by capillary pressure. Figure 15b illustrates a simple schematic of this step, where the residual layer adjacent to the upper wall is at the verge of break up. We may postulate that the air-Carbopol interface is non-uniform and wavy, due to the growth of perturbations of various wavelengths on the surface of the residual layer; see [23,45,51] for conceptually comparable phenomena in completely different contexts. In Fig. 15b, \hat{R} indicates the local principal radius of the curvature of the sinusoidal perturbation waves. According to the Young-Laplace equation ($\Delta \hat{p} = \hat{\sigma} / \hat{R}$), the smaller the radius of curvature, the higher the pressure jump across the interface. We postulate that at this step, the radius is small so that capillary pressure at certain places is sufficiently large to rupture the weakened structure bonds, which, in return, leads to the break up of the residual layers. This results in the formation of several Carbopol pieces on the upper/lower walls of the channel.

The descriptions presented are compatible with our experimental observations in that at low Carbopol concentrations, the Carbopol layer naturally has a weaker bonding strength, causing the residual layers to break up more easily. For higher Carbopol concentrations, the bonding strength is enhanced [79]; therefore, the residual layer is able to resist the break up. Higher air imposed flow rates also increase the wall shear stresses, which may weaken the bonding strength of the Carbopol gel.

The network structure regime may be similar to the film rupture phenomena in which the thin polymer film rupture is caused by capillary pressure, usually when the film thickness is very small [56,73,86]. Similar to the break up of residual layers, the film rupture processes in thin polymer films may lead to form diverse morphologies. Similar to the network structure regime, pattern forma-

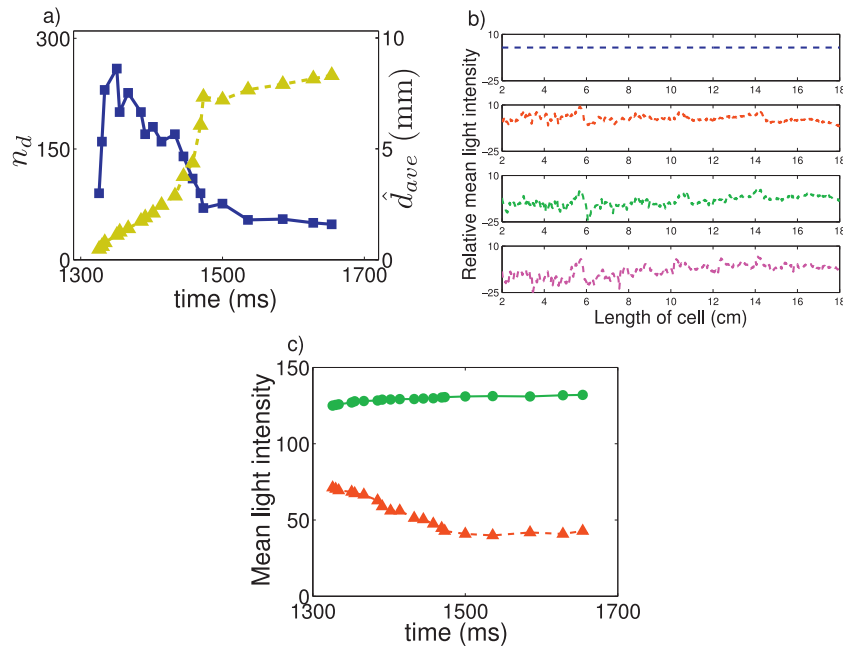


Fig. 16. a) Variation in the total number of cavities (■) and the mean characteristic diameter of cavities (▲) versus time, in the network structure regime, for the same experiment as in Fig. 14. b) Variation in relative mean light intensity versus length of cell for 4 sequential images of Fig. 14. c) Variation in mean light intensity of cavities (●) and Carbolpol pieces (▲) versus time.

tions through the film rupture depend on the polymer composition (or concentration) and the film thickness.

In order to provide further understanding about the network structure regime, characterizing the cavities versus time is useful. Figure 16a illustrates the variation in the number and the mean characteristic diameter of cavities versus time for a typical experiment, for which images are processed. It is interesting to note that the number of cavities is not monotonic versus time. Initially the cavities are quickly formed as the residual layer breaks into smaller pieces but the cavities eventually meet and merge with one another. The number of cavities stabilizes at a small plateau value as the network structure appears. On the other hand, the mean characteristic diameter of the cavities continuously increases and it finally reaches a nearly constant value.

The presence of cavities creates a highly non-uniform residual layer, to which we have also looked. Figure 16b shows the relative transverse mean light intensities in the finger domain for the 4 sequential images presented in Fig. 14, for which the images were converted to gray levels (between 0 to 255). The first image in Fig. 14 has been taken as a reference, to which the relative mean light intensities are compared. Comparing the top and bottom plots in Fig. 16, and considering that the film layer thickness is proportional to the light intensity, it can be concluded that the residual layers are highly non-uniform.

In order to gain insight about the thickness of Carbolpol pieces, Fig. 16c shows the variation of the mean light intensities of 10 areas, each covering 10×10 pixels randomly distributed in either the cavity area or the Carbolpol pieces area, versus time. This figure shows that while the mean light intensity of cavities is almost constant, the mean light intensity of Carbolpol pieces decreases initially with time but finally reaches a plateau value. This implies that the overall thickness of Carbolpol pieces increases but eventually becomes constant.

Various areas in the finger domain can be observed in the network structure regime. In order to observe these areas more clearly, a sequence of images was obtained at 1000 (fps) and plotted in Fig. 17. The experiment was conducted with MCC at a very

high imposed air flow rate (a video corresponding to this experiment is included in supplementary materials). In these images, 4 areas, marked by Roman numbers, can be distinguished. The first area (I) consists of the finger domain where thin wall layers are present. The second area (II) corresponds to a cavity formed on one of the walls. In the third area (III), cavities on both walls are observed. The fourth area (IV) corresponds to pieces of Carbolpol that are formed.

Based on the descriptions mentioned earlier, it may be expected that the values of surface tension and the bonding strength of Carbolpol (which is very loosely speaking proportional to the yield stress) to be the important parameters that delineate the boundary to the network structure regime. Therefore, at least Ca and Bn may be considered as the relevant dimensionless groups. Figure 18 plots the experimental data points in the plane of Ca versus Bn . Interestingly, the data belonging to the network structure regime are clearly segregated from the rest of the data in this figure. The transition seems to follow a line indicated by $Ca = 0.86Bn^{-2.82}$.

5. Summary

We have considered the Saffman–Taylor for non-Newtonian fluids in the Hele–Shaw cell. In this work, air displaced a Carbolpol gel, which exhibits both viscoplastic and viscoelastic properties, in addition to shear-thinning effects. The problem is complex as a result of many important dimensionless numbers involved, i.e., the Bingham number (Bn), the capillary number (Ca), the Weber number We , the Weissenberg number (Wi), the aspect ratio (δ), and power-law index (n). We identify three distinct flow regimes: a yield stress regime, a viscous regime and an elasto-inertial regime, based on the morphological differences and finger width variations. These flow regimes and their transition boundaries are studied in depth. We have succeeded to provide a clear picture of the flow over a reasonable range of dimensionless groups. Some of the secondary features of the flow have been also discussed, including the thickness of the residual wall layers as well as an interesting novel pattern, termed the network structure regime. Table 4 pro-

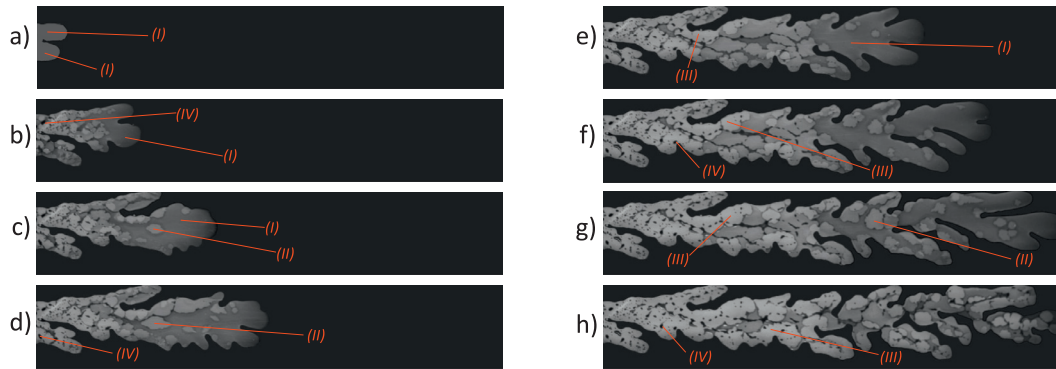


Fig. 17. Image sequence showing the finger evolution in the network structure regime. Different areas are explained in the text.

Table 4
Important dimensionless groups that the present study has delivered.

Dimensionless group	Significance	Critical value
We_c^*	Transition to inertial effects	76.5
$Ca \delta^{1+n} / (Bn - 0.5) : Bn > 0.5$	Transition between the yield stress and viscous regimes	550
Wi	Transition to elastic effects	0.13
$1/\lambda \delta^{1+n}$	Finger width plateau value	0.026
Ca^*	Enable collapse of λ from the viscous & elasto-inertial regimes	-
$\delta^{-2/3} (Ca Bn^*)^{-1/3}$	Enable collapse of λ from the yield stress regime	-
$t \approx h_{circ} - \frac{0.024}{Ca} + \frac{0.098}{Ca^2} - \frac{0.126}{Ca^3}$	Predict mean static residual wall layer thickness	-
$Ca Bn^{2.82}$	Transition from the network structure regime	0.86

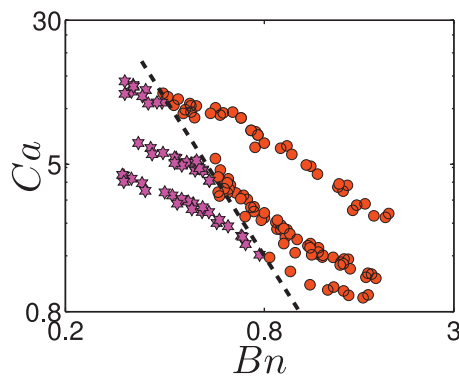


Fig. 18. A secondary flow regime classification based on the formation of a network structure inside the finger domain. The data correspond to the experiments for the network structure regime are marked by \star and the ones without by \bullet . The black dashed line indicates transition between the two regimes: $Ca = 0.86 Bn^{-2.82}$.

vides a summary of the main dimensionless groups that our work has delivered to predict various flow features.

Acknowledgments

This research has been carried out at Laval University, supported financially by the Discovery Grant of the Natural Sciences and Engineering Research Council of Canada (NSERC) and the Canada Foundation for Innovation (CFI). We thank Professor D. Rodrigue (Laval University) for allowing the access to the rheometer. We greatly thank Professor I. Frigaard (University of British Columbia) and Dr. R. Mollaabbasi (Laval University) for very useful discussions.

Supplementary material

Supplementary material associated with this article can be found, in the online version, at [10.1016/j.jnnfm.2017.03.007](https://doi.org/10.1016/j.jnnfm.2017.03.007).

This supplementary section includes two parts:

- Three videos showing the three main flow regimes: These videos show the finger evolution and the appearance of different flow patterns. The videos correspond to the experiment with $\hat{b} = 1.5$ mm & HCC. I) The yield stress regime: the mean imposed velocity is $\hat{V} = 1.8$ mm/s while the finger tip velocity is $\hat{U} = 8.3$ mm/s. The field of view is 20.8×4.3 cm². II) The viscous regime: the mean imposed velocity is $\hat{V} = 8.6$ mm/s while the finger tip velocity is $\hat{U} = 95.5$ mm/s. The field of view is 19.6×3.7 cm². III) The elasto-inertial regime: the mean imposed velocity is $\hat{V} = 41.7$ mm/s while the finger tip velocity is $\hat{U} = 215.2$ mm/s. The field of view is 20.2×4.1 cm².
- A video showing the network structure regime: The mean imposed velocity is $\hat{V} = 274$ mm/s while the finger tip velocity is $\hat{U} = 1068$ mm/s. The images correspond to the experiment with $\hat{b} = 0.9$ mm & MCC. The field of view is 24.6×6.7 cm².

References

- [1] T.T. Al-Housseiny, P.A. Tsai, H.A. Stone, Control of interfacial instabilities using flow geometry, *Nat. Phys.* 8 (10) (2012) 747–750.
- [2] M. Allouche, I. Frigaard, G. Sona, Static wall layers in the displacement of two visco-plastic fluids in a plane channel, *J. Fluid Mech.* 424 (1) (2000) 243–277.
- [3] M.B. Amar, E.C. Poire, Pushing a non-Newtonian fluid in a Hele-Shaw cell: from fingers to needles, *Phys. Fluids* 11 (7) (1999) 1757–1767.
- [4] E. Ben-Jacob, R. Godbey, N.D. Goldenfeld, J. Koplik, H. Levine, T. Mueller, L.M. Sander, Experimental demonstration of the role of anisotropy in interfacial pattern formation, *Phys. Rev. Lett.* 55 (12) (1985) 1315.
- [5] E. Ben-Jacob, H. Shmueli, O. Shochet, A. Tenenbaum, Adaptive self-organization during growth of bacterial colonies, *Physica A* 187 (3) (1992) 378–424.
- [6] D. Bensimon, L.P. Kadanoff, S. Liang, B.I. Shraiman, C. Tang, Viscous flows in two dimensions, *Rev. Mod. Phys.* 58 (4) (1986) 977.
- [7] S.H. Bittleston, J. Ferguson, I.A. Frigaard, Mud removal and cement placement during primary cementing of an oil well—Laminar non-Newtonian displacements in an eccentric annular Hele-Shaw cell, *J. Eng. Math.* 43 (2–4) (2002) 229–253.
- [8] J. Boujlel, P. Coussot, Measuring the surface tension of yield stress fluids, *Soft Matter* 9 (25) (2013) 5898–5908.
- [9] R. Brandao, J.V. Fontana, J.A. Miranda, Interfacial pattern formation in confined power-law fluids, *Phys. Rev. E* 90 (1) (2014) 013013.
- [10] F.P. Bretherton, The motion of long bubbles in tubes, *J. Fluid Mech* 10 (2) (1961) 166–188.

- [11] A. Buka, P. Palffy-Muhoray, Z. Racz, Viscous fingering in liquid crystals, *Phys. Rev. A* 36 (8) (1987) 3984–3989.
- [12] C. Chevalier, M.B. Amar, D. Bonn, A. Lindner, Inertial effects on Saffman–Taylor viscous fingering, *J. Fluid Mech.* 552 (2006) 83–97.
- [13] T. Chevalier, C. Chevalier, X. Clain, J.C. Dupla, J. Canou, S. Rodts, P. Coussot, Darcy's law for yield stress fluid flowing through a porous medium, *J. non-Newtonian Fluid Mech.* 195 (2013) 57–66.
- [14] R.L. Chuoke, P. Van Meurs, C. van der Poel, The instability of slow, immiscible, viscous liquid–liquid displacements in permeable media, *Trans. AIME* 216 (1959) 188–194.
- [15] Y. Cinar, A. Riaz, H.A. Tchelepi, et al., Experimental study of CO₂ injection into saline formations, *SPE ATCE*, 2007.
- [16] Y. Couder, N. Gerard, M. Rabaud, Narrow fingers in the Saffman–Taylor instability, *Phys. Rev. A* 34 (6) (1986) 5175.
- [17] P. Coussot, Saffman–Taylor instability in yield-stress fluids, *J. Fluid Mech.* 380 (1999) 363–376.
- [18] D.Q.M. Craig, S. Tamburic, G. Buckton, J.M. Newton, An investigation into the structure and properties of Carbopol 934 gels using dielectric spectroscopy and oscillatory rheometry, *J. Controlled Release* 30 (3) (1994) 213–223.
- [19] M.M. Cross, Relation between viscoelasticity and shear-thinning behaviour in liquids, *Rheol. Acta* 18 (5) (1979) 609–614.
- [20] Y. Dimakopoulos, J. Tsamopoulos, Transient displacement of a viscoplastic material by air in straight and suddenly constricted tubes, *J. non-Newtonian Fluid Mech.* 112 (1) (2003) 43–75.
- [21] B. Ebrahimi, P. Mostaghimi, H. Gholamian, K. Sadeghy, Viscous fingering in yield stress fluids: a numerical study, *J. Eng. Math.* (2015) 1–16.
- [22] B. Ebrahimi, S.M. Taghavi, K. Sadeghy, Two-phase viscous fingering of immiscible thixotropic fluids: a numerical study, *J. Non-Newton. Fluid Mech.* 218 (2015) 40–52.
- [23] J. Eggers, E. Villermaux, Physics of liquid jets, *Rep. Prog. Phys.* 71 (3) (2008) 036601.
- [24] P. Fast, L. Kondic, M.J. Shelley, P. Palffy-Muhoray, Pattern formation in non-Newtonian Hele–Shaw flow, *Phys. Fluids* 13 (5) (2001) 1191–1212.
- [25] J.V. Fontana, E.O. Dias, J.A. Miranda, Controlling and minimizing fingering instabilities in non-Newtonian fluids, *Phys. Rev. E* 89 (1) (2014) 013016.
- [26] J.F. Freitas, E.J. Soares, R.L. Thompson, Viscoplastic-viscoplastic displacement in a plane channel with interfacial tension effects, *Chem. Eng. Sci.* 91 (2013) 54–64.
- [27] P. Gondret, M. Rabaud, Shear instability of two-fluid parallel flow in a Hele–Shaw cell, *Phys. Fluids* 9 (11) (1997) 3267–3274.
- [28] S. Hill, et al., Channeling in packed columns, *Chem. Eng. Sci.* 1 (6) (1952) 247–253.
- [29] K.E. Holloway, P. Habdas, N. Semsarillar, K. Burfitt, J.R. de Bruyn, Spreading and fingering in spin coating, *Phys. Rev. E* 75 (4, 2) (2007) 046308.
- [30] G.M. Homsy, Viscous fingering in porous media, *Annu. Rev. Fluid Mech.* 19 (1) (1987) 271–311.
- [31] P.C. Huzyak, K.W. Koelling, The penetration of a long bubble through a viscoelastic fluid in a tube, *J. non-Newtonian Fluid Mech.* 71 (1) (1997) 73–88.
- [32] J. Ignes-Mullol, H. Zhao, J.V. Maher, Velocity fluctuations of fracturelike disruptions of associating polymer solutions, *Phys. Rev. E* 51 (2) (1995) 1338–1343.
- [33] N. Kagei, D. Kanie, M. Kawaguchi, Viscous fingering in shear thickening silica suspensions, *Phys. Fluids* 17 (2005) 0545103.
- [34] D.A. Kessler, J. Koplik, H. Levine, Pattern selection in fingered growth phenomena, *Adv. Phys.* 37 (3) (1988) 255–339.
- [35] J.Y. Kim, J.Y. Song, E.J. Lee, S.K. Park, Rheological properties and microstructures of Carbopol gel network system, *Colloid. Polym. Sci.* 281 (7) (2003) 614–623.
- [36] L. Kondic, P. Palffy-Muhoray, M.J. Shelley, Models of non-Newtonian Hele–Shaw flow, *Phys. Rev. E* 54 (5) (1996) R4536.
- [37] L. Kondic, M.J. Shelley, P. Palffy-Muhoray, Non-Newtonian Hele–Shaw flow and the Saffman–Taylor instability, *Phys. Rev. Lett.* 80 (7) (1998) 1433.
- [38] C.H. Lee, V. Moturi, Y. Lee, Thixotropic property in pharmaceutical formulations, *J. Controlled Release* 136 (2) (2009) 88–98.
- [39] E. Lemaire, P. Levitz, G. Daccord, H. Van Damme, From viscous fingering to viscoelastic fracturing in colloidal fluids, *Phys. Rev. Lett.* 67 (15) (1991) 2009.
- [40] S. Li, J.S. Lowengrub, J. Fontana, P. Palffy-Muhoray, Control of viscous fingering patterns in a radial Hele–Shaw cell, *Phys. Rev. Lett.* 102 (17) (2009) 174501.
- [41] A. Lindner, D. Bonn, J. Meunier, Viscous fingering in a shear-thinning fluid, *Phys. Fluids* 12 (2) (2000) 256–261.
- [42] A. Lindner, D. Bonn, E.C. Poire, M.B. Amar, J. Meunier, Viscous fingering in non-Newtonian fluids, *J. Fluid Mech.* 469 (2002) 237–256.
- [43] A. Lindner, P. Coussot, D. Bonn, Viscous fingering in a yield stress fluid, *Phys. Rev. Lett.* 85 (2) (2000) 314.
- [44] A. Lindner, P. Coussot, D. Bonn, Viscous fingering in a gel, in: *Branching in Nature*, Springer, 2001, pp. 433–438.
- [45] D. Lukas, N. Pan, A. Sarkar, M. Weng, J. Chaloupek, E. Kostakova, L. Ocheretna, P. Mikes, M. Pociute, E. Amler, Auto-model based computer simulation of Plateau–Rayleigh instability of mixtures of immiscible liquids, *Physica A* 389 (11) (2010) 2164–2176.
- [46] N. Maleki-Jirsarai, A. Lindner, S. Rouhani, D. Bonn, Saffman–Taylor instability in yield stress fluids, *J. Phys. Condens. Matter* 17 (14) (2005) S1219.
- [47] S. Malhotra, M.M. Sharma, Impact of fluid elasticity on miscible viscous fingering, *Chem. Eng. Sci.* 117 (2014) 125–135.
- [48] D.S. Malkus, J.A. Nohel, B.J. Plohr, Analysis of new phenomena in shear flow of non-Newtonian fluids, *SIAM J. Appl. Math.* 51 (4) (1991) 899–929.
- [49] K.V. McCloud, J.V. Maher, Experimental perturbations to Saffman–Taylor flow, *Phys. Rep.* 260 (3) (1995) 139–185.
- [50] J.W. McLean, P.G. Saffman, The effect of surface tension on the shape of fingers in a Hele–Shaw cell, *J. Fluid Mech.* 102 (1981) 455–469.
- [51] J. Meyer, D. Weihs, Capillary instability of an annular liquid jet, *J. Fluid Mech.* 179 (6) (1987) 531–545.
- [52] T.G. Mezger, *The Rheology Handbook: For Users of Rotational and Oscillatory Rheometers*, Vincentz Network GmbH & Co KG, 2006.
- [53] K.B. Migler, H. Hervet, L. Leger, Slip transition of a polymer melt under shear stress, *Phys. Rev. Lett.* 70 (3) (1993) 287.
- [54] R. Mollaabbasi, S.M. Taghavi, Buoyant displacement flows in slightly non-uniform channels, *J. Fluid Mech.* 795 (2016) 876–913.
- [55] S. Mora, M. Manna, Saffman–Taylor instability for generalized newtonian fluids, *Phys. Rev. E* 80 (1) (2009) 016308.
- [56] G. Narsimhan, E. Ruckenstein, Effect of bubble size distribution on the enrichment and collapse in foams, *Langmuir* 2 (4) (1986) 494–508.
- [57] J. Nase, D. Derks, A. Lindner, Dynamic evolution of fingering patterns in a lifted Hele–Shaw cell, *Phys. Fluids* 23 (12) (2011) 123101.
- [58] S. Nguyen, R. Folch, V.K. Verma, H. Henry, M. Plapp, Phase-field simulations of viscous fingering in shear-thinning fluids, *Phys. Fluids* 22 (10) (2010) 103102.
- [59] J. Nittmann, G. Daccord, H.E. Stanley, Fractal growth of viscous fingers: quantitative characterization of a fluid instability phenomenon, *Nature* 314 (6007) (1985) 141–144.
- [60] F.M. Orr, J.J. Taber, Use of carbon dioxide in enhanced oil recovery, *Science* 224 (4649) (1984) 563–569.
- [61] C.W. Park, G.M. Homsy, Two-phase displacement in Hele–Shaw cells: theory, *J. Fluid Mech.* 139 (1984) 291–308.
- [62] H. Pascal, Rheological behaviour effect of non-Newtonian fluids on dynamic of moving interface in porous media, *Int. J. Eng. Sci.* 22 (3) (1984) 227–241.
- [63] J.M. Piau, Carbopol gels: Elastoviscoplastic and slippery glasses made of individual swollen sponges: meso- and macroscopic properties, constitutive equations and scaling laws, *J. non-Newtonian Fluid Mech.* 144 (1) (2007) 1–29.
- [64] D. Pihler-Puzovic, P. Illien, M. Heil, A. Juel, Suppression of complex fingerlike patterns at the interface between air and a viscous fluid by elastic membranes, *Phys. Rev. Lett.* 108 (6) (2012) 074502.
- [65] E.C. Poire, M.B. Amar, Finger behavior of a shear thinning fluid in a Hele–Shaw cell, *Phys. Rev. Lett.* 81 (10) (1998) 2048.
- [66] A.J. Posilinski, P.R. Oehler, V.K. Stokes, Isothermal gas-assisted displacement of viscoplastic liquids in tubes, *Polym. Eng. Sci.* 35 (11) (1995) 877–892.
- [67] M. Rabaud, Y. Couder, N. Gerard, Dynamics and stability of anomalous Saffman–Taylor fingers, *Phys. Rev. A* 37 (3) (1988) 935.
- [68] A. Rathapon, A. Sirivat, P. Vayumhasuwan, others, Viscoelastic properties of Carbopol 940 gels and their relationships to piroxicam diffusion coefficients in gel bases, *Pharm. Res.* 22 (12) (2005) 2134–2140.
- [69] D.A. Reinelt, P.G. Saffman, The penetration of a finger into a viscous fluid in a channel and tube, *SISC* 6 (3) (1985) 542–561.
- [70] G. Rousseaux, A. De Wit, M. Martin, Viscous fingering in packed chromatographic columns: linear stability analysis, *J. Chromatogr. A* 1149 (2) (2007) 254–273.
- [71] C. Ruyer-Quil, Inertial corrections to the darcy law in a Hele–Shaw cell, *C R Acad. Sci. IIb Mec.* 329 (5) (2001) 337–342.
- [72] P.G. Saffman, G. Taylor, The penetration of a fluid into a porous medium or Hele–Shaw cell containing a more viscous liquid, in: *Proceedings of the Royal Society A*, 245, 1958, pp. 312–329.
- [73] A. Sehgal, V. Ferreiro, J.F. Douglas, E.J. Amis, A. Karim, Pattern-directed dewetting of ultrathin polymer films, *Langmuir* 18 (18) (2002) 7041–7048.
- [74] P.A.P. Swain, G. Karapetsas, O.K. Matar, K.C. Sahu, Numerical simulation of pressure-driven displacement of a viscoplastic material by a Newtonian fluid using the lattice Boltzmann method, *Eur. J. Mech. B-Fluid* 49 (2015) 197–207.
- [75] P. Tabeling, A. Libchaber, Film draining and the Saffman–Taylor problem, *Phys. Rev. A* 33 (1) (1986) 794.
- [76] P. Tabeling, G. Zocchi, A. Libchaber, An experimental study of the Saffman–Taylor instability, in: *Physicochemical Hydrodynamics*, Springer, 1988, pp. 515–525.
- [77] G.I. Taylor, Cavitation of a viscous fluid in narrow passages, *J. Fluid Mech.* 16 (04) (1963) 595–619.
- [78] R.L. Thompson, E.J. Soares, Viscoplastic dimensionless numbers, *J. Non-Newton. Fluid Mech.* (2016).
- [79] P.H.T. Uhlherr, J. Guo, C. Tiu, X.M. Zhang, J.Z.Q. Zhou, T.N. Fang, The shear-induced solid–liquid transition in yield stress materials with chemically different structures, *J. non-Newtonian Fluid Mech.* 125 (2) (2005) 101–119.
- [80] H. Van Damme, E. Alsac, C. Laroche, L. Gatineau, On the respective roles of low surface tension and non-Newtonian rheological properties in fractal fingering, *Europhys. Lett.* 5 (1) (1988) 25.
- [81] H. Van Damme, E. Lemaire, Y. Ould, M. Abdelhaye, A. Mourchid, P. Levitz, Pattern formation in particulate complex fluids: A guided tour, in: *Non-Linearity and Breakdown in Soft Condensed Matter*, Springer, 1994, pp. 134–150.
- [82] S.J. Weinstein, E.B. Dussan, L.H. Ungar, A theoretical study of two-phase flow through a narrow gap with a moving contact line: viscous fingering in a Hele–Shaw cell, *J. Fluid Mech.* 221 (1990) 53–76.
- [83] A.R. White, T. Ward, Constant pressure gas-driven displacement of a shear-thinning liquid in a partially filled radial Hele–Shaw cell: thin films, bursting and instability, *J. non-Newtonian Fluid Mech.* 206 (2014) 18–28.
- [84] K. Wielage-Burchard, I.A. Frigaard, Static wall layers in plane channel displacement flows, *J. non-Newtonian Fluid Mech.* 166 (5) (2011) 245–261.

- [85] R.A. Wooding, H.J. Morel-Seytoux, Multiphase fluid flow through porous media, *Annu. Rev. Fluid Mech.* 8 (1) (1976) 233–274.
- [86] T. Xia, Y. Qin, Y. Huang, T. Huang, J. Xu, Y. Li, Sequence control of phase separation and dewetting in PS/PVME blend thin films by changing molecular weight of PS, *J. Chem. Phys.* 145 (20) (2016) 204903.
- [87] J. Zilz, C. Schafer, C. Wagner, R.J. Poole, M.A. Alves, A. Lindner, Serpentine channels: micro-rheometers for fluid relaxation times, *Lab. Chip.* 14 (2) (2014) 351–358.
- [88] G. Zocchi, B.E. Shaw, A. Libchaber, L.P. Kadanoff, Finger narrowing under local perturbations in the Saffman–Taylor problem, *Phys. Rev. A* 36 (4) (1987) 1894.